1   **Arctic Ocean CO$_2$ uptake: an improved multi-year estimate of the air–sea CO$_2$ flux**

2   **incorporating chlorophyll-a concentrations**

4   Sayaka Yasunaka[1,2], Eko Siswanto[1], Are Olsen[3], Mario Hoppema[4], Eiji Watanabe[2],

5   Agneta Fransson[5], Melissa Chierici[6], Akihiko Murata[1,2], Siv K. Lauvset[3,7], Rik

6   Wanninkhof[8], Taro Takahashi[9], Naohiro Kosugi[10], Abdirahman M. Omar[7], Steven van

7   Heuven[11], and Jeremy T. Mathis[12]

9   [1]Research and Development Center for Global Change, Japan Agency for Marine-Earth

10   Science and Technology, Yokosuka, Japan

11   [2]Institute of Arctic Climate and Environment Research, Japan Agency for Marine-Earth

12   Science and Technology, Yokosuka, Japan

13   [3]Geophysical Institute, University of Bergen and Bjerknes Centre for Climate Research,

14   Bergen, Norway

15   [4]Alfred Wegener Institute Helmholtz Centre for Polar and Marine Research, Climate

16   Sciences Department, Bremerhaven, Germany

17   [5]Norwegian Polar Institute, Fram Centre, Norway

18   [6]Institute of Marine Research, Tromsø, Norway

19   [7]Uni Research Climate, Bjerknes Centre for Climate Research, Bergen, Norway

20   [8] National Oceanic and Atmospheric Administration, Atlantic Oceanographic and

21   Meteorological Laboratory, Miami, FL, USA

22   [9]Lamont-Doherty Earth Observatory of Columbia University, Palisades, NY, USA

23   [10]Oceanography and Geochemistry Research Department, Meteorological Research

24   Institute, Japan Meteorological Agency, Tsukuba, Japan

25   [11]Energy and Sustainability Research Institute Groningen, Groningen University, The

26   Netherlands

27   [12] National Oceanic and Atmospheric Administration, Arctic Research Program, Seattle,

28   WA, USA

30   **Abstract**

31   We estimated monthly air–sea CO_2 fluxes in the Arctic Ocean and its adjacent seas

32   north of 60° N from 1997 to 2014. This was done by mapping partial pressure of CO_2 in

33   the surface water ($p\text{CO}_{2w}$) using a self-organizing map (SOM) technique incorporating

34   chlorophyll-a concentration (Chl-a), sea surface temperature, sea surface salinity, sea ice

35   concentration, atmospheric CO_2 mixing ratio, and geographical position. We applied

36   new algorithms for extracting Chl-a from satellite remote sensing reflectance with close

37 examination of uncertainty of the obtained Chl-a values. The overall relationship

38 between $p\text{CO}_{2\text{w}}$ and Chl-a was negative, whereas the relationship varied among seasons

39 and regions. The addition of Chl-a as a parameter in the SOM process enabled us to

40 improve the estimate of $p\text{CO}_{2\text{w}}$ particularly via better representation of its decline in

41 spring which resulted from biologically mediated $p\text{CO}_{2\text{w}}$ reduction. As a result of the

42 inclusion of Chl-a, the uncertainty in the CO_2 flux estimate was reduced, with a net

43 annual Arctic Ocean CO_2 uptake of 180 ± 130 TgC y^{-1}. Seasonal to interannual

44 variation of the CO_2 influx was also figured out.

46 **1. Introduction**

47 The Arctic Ocean and its adjacent seas (Fig. 1) generally act as a sink for atmospheric

48 CO_2 because of the high solubility of CO_2 in their low-temperature waters, combined

49 with extensive primary production during the summer season (Bates and Mathis, 2009).

50 The Arctic Ocean and its adjacent seas consist of complicated subregions that include

51 continental shelves, central basins, and sea-ice-covered areas. Therefore, the surface

52 partial pressure of CO_2 ($p\text{CO}_{2\text{w}}$) distribution is not only affected by ocean heat loss and

53 gain, and biological production and respiration, but also by sea-ice formation and

54 melting, river discharge, and shelf–basin interactions (cf. Bates and Mathis, 2009, and

55   references therein). However, CO_2 measurements are sparse in this very heterogeneous

56   area (Fig. 2), and hence the existing air–sea CO_2 flux estimates in the Arctic are poorly

57   constrained (Bates and Mathis, 2009; Schuster et al., 2013; Yasanuka et al., 2016).

58   As global warming progresses, melting of sea ice will increase the area of open water

59   and enhance the potential for atmospheric CO_2 uptake (e.g., Bates et al., 2006; Gao et

60   al., 2012). However, other processes could suppress CO_2 uptake. For example,

61   increasing seawater temperatures, declining buffer capacity due to the freshening of

62   Arctic surface water by increased river runoff and melting of sea-ice, and increased

63   vertical mixing supplying high-CO_2 water to the surface will all result in a tendency for

64   reduced uptake (Bates and Mathis, 2009; Cai et al., 2010; Chierici et al., 2011; Else et

65   al., 2013; Bates et al. 2014; Fransson et al., 2017). The combined effect of all these

66   processes on ocean CO_2 uptake has not yet been clarified for the Arctic.

67   Yasunaka et al. (2016) prepared monthly maps of air–sea CO_2 fluxes from 1997 to

68   2013 for the Arctic north of 60° N by applying, for the first time, a self-organizing map

69   (SOM) technique to map pCO_{2w} in the Arctic Ocean. The advantage of the SOM

70   technique is its ability to empirically determine relationships among variables without

71   making any a priori assumptions (about what types of regression functions are

72   applicable, and for which sub-regions the same regression function can be adopted, for

73   example). The SOM technique has been shown to reproduce the distribution of $p\text{CO}_{2\text{w}}$

74   from unevenly distributed observations better than multiple regression methods

75   (Lefèvre et al., 2005; Telszewski et al., 2009). The uncertainty of the CO_2 flux estimated

76   by Yasunaka et al. (2016), however, was large (±3.4–4.6 mmol m^{-2} d^{-1}), and the

77   estimated CO_2 uptake in the Arctic Ocean was smaller than the uncertainty (180 ± 210

78   TgC y^{-1}). One possible reason for the large uncertainties is that no direct proxies for the

79   effect of biological processes on $p\text{CO}_{2\text{w}}$ were used in that study, leading to an

80   underestimation of the seasonal amplitude of $p\text{CO}_{2\text{w}}$.

81   Remotely sensed chlorophyll-a concentrations (Chl-a) has been used in several

82    $p\text{CO}_{2\text{w}}$ mapping efforts as a direct proxy for the effect of primary production. For

83   example Chierici et al. (2009) produced $p\text{CO}_{2\text{w}}$ algorithms for the subpolar North

84   Atlantic during the period from May to October and found that the inclusion of Chl-a

85   improved the fit substantially. Measurements in several areas of the Arctic show that

86   relationships between $p\text{CO}_{2\text{w}}$ and Chl-a occur also in this region. They correlate

87   negatively (Gao et al., 2012; Ulfsbo et al., 2014), as expected from the drawdown of

88   CO_2 during photosynthesis, but exceptions do occur; in coastal regions the correlation is

89   positive (Mucci et al., 2010).

90   Several studies have demonstrated that Chl-a in the Arctic can be estimated from

91   satellite remote sensing reflectance (Rrs) (e.g. Arrigo and Dijken, 2004; Cota et al.,

92   2004). Perrette et al. (2011) showed that satellite-derived Chl-a successfully captured a

93   phytoplankton bloom in the ice-edge region. Changes in the seasonal cycle from a

94   single peak to a double peak of Chl-a have also been detected and are likely a

95   consequence of the recent sea-ice loss in the Arctic (Ardyna et al., 2014). However, the

96   available products (e.g. NASA's OceanColor dataset) in the Arctic include large

97   uncertainty and many missing values because of sea ice, low angle of sun-light and

98   cloud cover, and are also prone to error due to the co-occurrence of large colored

99   dissolved organic matter (CDOM) and total suspended matter (TSM) concentrations

100   (e.g., Matuoka et al., 2007; Lewis et al., 2016). Here we deal with these issues by using

101   several Chl-a algorithms optimised for the Arctic and others, and by excluding Chl-a

102   data from grid cells potentially affected by CDOM and TSM. Calculated Chl-a values

103   were then interpolated Chl-a so as to fit with the original data. Using these data, we

104   examined the relationship between $p\mathrm{CO_{2w}}$ and Chl-a in the Arctic Ocean and its

105   adjacent seas, and computed monthly air–sea CO_2 flux maps for regions north of 60° N

106   using a SOM technique similar to that of Yasunaka et al. (2016), and with Chl-a added

107   to the SOM process.

108

109 **2. Data**

110 2.1. $p\mathrm{CO}_{2\,w}$ measurements

111 We used fugacity of CO_2 ($f\mathrm{CO}_{2w}$) observations from the Surface Ocean CO_2 Atlas

112 version 4 (SOCATv4; Bakker et al., 2016; http://www.socat.info/; 1,983,799 data points

113 from >60° N), and $p\mathrm{CO}_{2w}$ observations from the Global Surface $p\mathrm{CO}_2$ Database Version

114 2014 (LDEOv2014; Takahashi et al., 2015;

115 http://cdiac.ornl.gov/oceans/LDEO_Underway_Database/; 302,150 data points from

116 >60° N). In the LDEO database, $p\mathrm{CO}_{2w}$ is based on measured CO_2 mixing ratio in a

117 parcel of air equilibrated with sea-water sample, and computed assuming CO_2 as an

118 ideal gas, whereas in the SOCAT, $f\mathrm{CO}_2$ is obtained considering the non-ideality from

119 CO_2-CO_2 and CO_2-$\mathrm{H}_2\mathrm{O}$ molecular interactions. Because of ambiguities in the CO_2-$\mathrm{H}_2\mathrm{O}$

120 interaction corrections, the SOCAT $f\mathrm{CO}_{2w}$ values are converted to $p\mathrm{CO}_{2w}$ values (a

121 correction of <1 %), and then combined them with the LDEO $p\mathrm{CO}_{2w}$ values. When data

122 points were duplicated in the SOCAT and LDEO datasets, the SOCAT version was used,

123 except for the data obtained from onboard the USCGC *Healy* as these have been

124 reanalyzed by Takahashi et al. (2015). Altogether 200,409 duplicates were removed. We

125 also used shipboard $p\mathrm{CO}_{2w}$ data obtained during cruises of the R/V *Mirai* of the Japan

126 Agency for Marine-Earth Science and Technology (JAMSTEC) that have not yet been

127   included in SOCATv4 or LDEOv2014 (cruises MR09_03, MR10_05, MR12_E03, and

128   MR13_06; available at http://www.godac.jamstec.go.jp/darwin/e; 95,725 data points

129   from >60° N). In total, we used 2,181,265 pCO_{2w} data points, 33 % more than used by

130   Yasunaka et al. (2016).

131   To further improve the data coverage, especially for the ice-covered regions, we also

132   used 2166 pCO_{2w} values calculated from dissolved inorganic carbon (DIC) and total

133   alkalinity (TA) data extracted from the Global Ocean Data Analysis Project version 2

134   (GLODAPv2; Key et al., 2015; Olsen et al., 2016; http://www.glodap.info). 90% of

135   these data were obtained at cruises without underway pCO_{2w} data. We extracted values

136   of samples obtained from water depths shallower than 10 m, or the shallowest values

137   from the upper 30 m of each cast if there were no values from above 10 m. There are

138   1795 data points above 10 m depth, 296 in the 10–20 m range, and 75 in the 20–30 m

139   range. This resulted in 94 % more calculated pCO_{2w} values than used by Yasunaka et al.

140   (2016), and altogether the number of directly measured and calculated data points used

141   here is 33% more than used in Yasunaka et al. (2016). The CO2SYS program (Lewis

142   and Wallace, 1998; van Heuven et al., 2009) was used for the calculation with the

143   dissociation constants reported by Lueker et al. (2000) and Dickson (1990).

144   We checked the difference between calculated pCO_{2w} and measured pCO_{2w} using the

145   data from cruises with both bottle DIC/TA samples and underway pCO_{2w} available

146   (10% of the bottle samples, i.e., 245 pairs). Mean value for the calculated pCO_{2w} values

147   from bottle DIC/TA samples from the upper 30 m was 299 ± 42 µatm, and that for the

148   corresponding directly measured pCO_{2w} values from underway observation generally at

149   4–6m was 289 ± 11 µatm. The mean values are slightly higher for calculated pCO_{2w}

150   values than for measured ones, but the difference is smaller than the standard deviation

151   and the uncertainties of the calculation (the latter of which is 14 µatm; see Section 4.2).

152   The difference between calculated and measured pCO_{2w} is not dependent on the depth

153   where the TA/DIC samples were obtained. It was 10 ± 31 µatm for samples from above

154   10 m, 7 ± 27 µatm for samples from 10–20 m, and 11 ± 47 µatm for samples from 20–

155   30 m.

156   The availability of pCO_{2w} data (measured and calculated) varies spatially and

157   temporally (Fig. 2). Most of the available data are from the subpolar North Atlantic, the

158   Greenland Sea, the Norwegian Sea, the Barents Sea, and the Chukchi Sea while much

159   less data are available for the Kara Sea, the Laptev Sea, the East Siberian Sea, and the

160   Eurasian Basin. The number of pCO_{2w} data increased after 2005, but there are also a

161   substantial number of data from before 2004.

162

163   2.2. Other data

164   To calculate Chl-a, we used merged Rrs data from the SeaWiFS, MODIS-Aqua, MERIS,

165   and VIIRS ocean color sensors processed and distributed by the GlobColour Project

166   (Maritorena et al., 2010; http://hermes.acri.fr/index.php?class=archive). For

167   compatibility with the spatio-temporal resolution of the gridded $p\mathrm{CO_{2w}}$ data (see below

168   Sect. 3.3), we selected monthly mean Rrs data with a spatial resolution of 1° (latitude) ×

169   1° (longitude).

170   Sea surface temperature (SST) data were extracted from the National Oceanic and

171   Atmospheric Administration (NOAA) Optimum Interpolation SST Version 2 (Reynolds

172   et al., 2002; http://www.esrl.noaa.gov/psd/data/gridded/data.noaa.oisst.v2.html). These

173   data are provided at a resolution of 1° × 1° × 1 month. Sea surface salinity (SSS) data

174   were retrieved from the Polar Science Center Hydrographic Climatology version 3.0,

175   which also has a resolution of 1° × 1°× 1 month (Steele et al., 2001;

176   http://psc.apl.washington.edu/nonwp_projects/PHC/Climatology.html). Sea ice

177   concentration (SIC) data were obtained from the NOAA/National Snow and Ice Data

178   Center Climate Data Record of Passive Microwave Sea Ice Concentration version 2,

179   which has a resolution of 25 km × 25 km × 1 month (Meier et al., 2013;

180   http://nsidc.org/data/G02202). These data were averaged into 1° × 1° × 1 month

181   grid-cells. Zonal mean data for the atmospheric CO_2 mixing ratio (xCO_{2a}) were

182   retrieved from the NOAA Greenhouse Gas Marine Boundary Layer Reference data

183   product (Conway et al., 1994; http://www.esrl.noaa.gov/gmd/ccgg/mbl/index.html) and

184   were interpolated into $1° \times 1° \times 1$ month grid-cells. Both sea level pressure and 6-hourly

185   10-m wind speeds data were obtained from the U.S. National Centers for Environmental

186   Prediction–Department of Energy Reanalysis 2 (NCEP 2) (Kanamitsu et al., 2002;

187   http://www.esrl.noaa.gov/psd/data/gridded/data.ncep.reanalysis2.html). We also used

188   the 6-hourly 10-m wind speeds from the U.S. National Centers for Atmospheric

189   Prediction and the National Center for Atmospheric Research Reanalysis 1 (NCEP1)

190   (Kalnay et al., 1996;

191   https://www.esrl.noaa.gov/psd/data/gridded/data.ncep.reanalysis.html) when the gas

192   transfer velocity was optimized for NCEP2 wind (see Section 3.5 below).

193   Surface nitrate measurements were extracted from GLODAPv2 (Key et al., 2015;

194   Olsen et al., 2016) and the World Ocean Database 2013 (WOD; Boyer et al., 2013).

195   When data points were duplicated in the GLODAPv2 and WOD datasets, the

196   GLODAPv2 version was used as this has been subjected to more extensive quality

197   control.

198

3. Methods

3.1. Calculation of chlorophyll-a concentrations

Chl-a was calculated from Rrs by using the Arctic algorithm developed by Cota et al.

(2004). Several assessments have shown that this algorithm has a large uncertainty (e.g.,

Matsuoka et al., 2007; Lewis et al., 2016), and therefore the sensitivity of our results to

this choice was evaluated by using two alternative algorithms for Chl-a: the standard

algorithm of O'Reilly et al. (1998), and the coastal algorithm, of Tassan (1994).

   To ensure that we were working with Rrs data relatively unaffected by CDOM and

TSM, the Chl-a data were masked following the method of Siswanto et al. (2013).

Briefly, the Rrs spectral slope between 412 and 555 nm ($Rrs_{555\text{-}412\ slope}$; $sr^{-1}\ nm^{-1}$) was

plotted against logarithmically transformed Chl-a. Based on the scatter plot of

log(Chl-a) and $Rrs_{555\text{-}412\ slope}$, we then defined a boundary line separating

phytoplankton-dominated grid-cells ($Rrs_{555\text{-}412\ slope}$ < boundary value) from potentially

non-phytoplankton-dominated grid-cells ($Rrs_{555\text{-}412\ slope} \geq$ boundary value) by:

$$Rrs_{555\text{-}412\ slope} = -0.000003\{\log(\text{Chl-a})\}^2 + 0.00002\{\log(\text{Chl-a})\} + 0.00006. \quad (1)$$

Grid-cells were considered invalid and masked out if 1) $Rrs_{555\text{-}412\ slope} \geq$ boundary value,

217   or 2) Rrs at 555nm (Rrs_{555}) > 0.01 sr^{-1} (or normalized water-leaving radiance > 2 mW

218   cm^{-2} μm^{-1} sr^{-1}; see Siswanto et al., 2011 and Moore et al., 2012). This criterion masked

219   2% of all Chl-a data.

220   The criteria described in the previous paragraph could mask out grid-cells having

221   coccolithophore blooms, which are sometimes observed in the Arctic Ocean (e.g.,

222   Smyth et al., 2004), as they also have Rrs_{555} > 0.01 sr^{-1} (Moore et al., 2012). Unlike

223   waters dominated by non-phytoplankton particles, whose Rrs spectral shape peaks at

224   555 nm, the Rrs spectral shape of waters with coccolithophore blooms peaks at 490 or

225   510 nm (see Iida et al., 2002; Moore et al., 2012). Therefore, grid-cells with Rrs spectral

226   peaks at 490 or 510 nm (already classified using the criteria of Rrs at 490nm (Rrs_{490}) >

227   Rrs at 443nm (Rrs_{443}) and Rrs at 510nm (Rrs_{510}) > Rrs_{555}) were considered as

228   coccolithophore grid-cells, and were reintroduced. 8% of the masked Chl-a data were

229   reintroduced by this criterion.

230

231   3.2. Chlorophyll-a interpolation

232   Chl-a values are often missing because of cloud cover, low angle of sunlight, or sea ice.

233   For the period and area analyzed here, data are missing for 86 % of the space and time

234   grid-cells. Because pCO_{2w} mapping requires a complete Chl-a field without missing

235   values, we interpolated the Chl-a data as follows; 1) Chl-a was set to 0.01 mg m^{-3}

236   (minimum value of Chl-a) in high-latitude regions in winter when there was no light

237   (north of 80° N in December and January, and north of 88° N in November and

238   February). 2) Whenever SIC was greater than 99 %, Chl-a was set to 0.01 mg m^{-3} (full

239   ice coverage, thus minimum Chl-a). We chose the strict criterion of SIC > 99 % because

240   weak but significant primary production has been found to occur under the sea ice in

241   regions with SIC around 90 % (Gosselin et al., 1997; Ulfsbo et al., 2014; Assmy et al.,

242   2017). 3) The remaining grid-cells with missing data were filled, wherever possible,

243   using the average of Chl-a in the surrounding grid-cells within ±1° latitude and ±1°

244   longitude; this mainly compensated for missing Chl-a values due to cloud cover or

245   grid-cells masked out as potentially affected by CDOM and TSM. 4) Parts of the

246   remaining missing Chl-a values, mainly for the pre-satellite period of January–August

247   1997, were set to the monthly climatological Chl-a values based on the 18-year monthly

248   mean from 1997 to 2014. 5) The final remaining missing Chl-a data, mainly for the

249   marginal sea-ice zone, were generated by linear interpolation using surrounding data.

250   With each interpolation step the number of the grid-cells with missing data decreased;

251   23 % of grid-cells without Chl-a data were filled by the first step, and the subsequent

252   steps provided data for the remaining 12, 8, 5, and 52 %.

253

254 3.3. Gridding of pCO_2 data

255 In order to bring the individual pCO_{2w} data to the same resolution as the other input data,

256 they were gridded to $1° \times 1° \times 1$ month grid-cells covering the years from 1997 to 2014.

257 This was carried out using the same three-step procedure of Yasunaka et al. (2016) as

258 this excludes values that deviate largely from the long-term mean in the area of each

259 grid cell. In short, first, anomalous values were screened in the following manner. We

260 calculated the long-term mean and its standard deviation for a window size of ±5° of

261 latitude, ±30° of longitude, and ±2 months (regardless of the year) for each $1° \times 1° \times 1$

262 month grid-cell. We then eliminated the data in each grid-cell that differed by more than

263 three standard deviations from this long-term mean. In the second step, we recalculated

264 the long-term mean and its standard deviation using a smaller window size of ±2° of

265 latitude, ±10° of longitude, and ±1 month (regardless of the year) for each $1° \times 1° \times 1$

266 month grid-cell, and eliminated data that differed from that long-term mean by more

267 than three standard deviations. In the final step the mean value of the remaining data in

268 each $1° \times 1° \times 1$ month grid cell for each year from 1997 to 2014 was calculated. This

269 procedure identified in total about 0.5 % of the data as extreme values. These may well

270 be correct observations, but likely reflect small spatial scale and/or short time scale

271   variations that can are quite atypical of the large-scale variability of interest in this study.

272   These excluded values were randomly distributed in time and space.

273   Although some studies have used pCO_{2w} normalized to a certain year, based on the

274   assumption of a constant rate of increase for pCO_{2w} (e.g., Takahashi et al., 2009), we

275   used "non-normalized" pCO_{2w} values from all years; therefore, in our analysis pCO_{2w}

276   can increase both non-linearly in time and non-uniformly in space.

277

278   3.4. pCO_2 estimation using a self-organizing map

279   We estimated pCO_{2w} by the SOM technique used by Yasunaka et al. (2016), but with

280   Chl-a as an added training parameter to the SOM in addition to SST, SSS, SIC, xCO_{2a},

281   and geographical position X (=sin[latitude] × cos[longitude]) and Y (=sin[latitude] ×

282   sin[longitude]). Chl-a, SST, SSS, and SIC are closely associated with processes causing

283   variation in pCO_{2w}, such as primary production, warming/cooling, mixing, and

284   freshwater input, and represent spatio-temporal pCO_{2w} variability at seasonal to

285   interannual time-scales. Including the xCO_{2a} enables the SOM to reflect the pCO_{2w}

286   time-trend in response to the atmospheric CO_2 changes including large seasonal

287   variation and continued anthropogenic emissions. In several previous studies the

288   anthropogenic pCO_{2w} increase has been assumed to be steady and homogeneous, and

289 subtracted from the original pCO_{2w} data and added to the estimated pCO_{2w} (Nakaoka et

290 al. 2013; Zheng et al. 2014). However, the occurrence of steady and homogeneous

291 pCO_{2w} trends has not yet been demonstrated in the Arctic Ocean and using xCO_{2a} as a

292 training parameter in the SOM, similar to Landschutzer et al. (2013, 2014) is preferable.

293 Finally, the inclusion of geographical position among the training parameters can

294 prevent systematic spatial biases (Yasunaka et al., 2014). Compared to other efforts

295 mapping pCO_{2w} using the SOM technique such as those by Telszewski et al. (2009) and

296 Nakaoka et al. (2013), we used xCO_{2a}, and geographical position as training parameters

297 while we did not use mixed layer depth because of lack of reliable data in the Arctic.

298   Briefly, the SOM technique was implemented as follows: first, the approximately one

299 million $1° \times 1° \times 1$ month grid-cells in the analysis region and period were assigned to

300 5000 groups, which are called "neurons", of the SOM by using the training parameters.

301 Then, each neuron was labeled, whenever possible, with the pCO_{2w} value of the

302 grid-cell where the Chl-a, SST, SSS, SIC, xCO_{2a}, and X and Y values were most similar

303 to those of the neuron. Finally, each grid-cell in the analysis region and period was

304 assigned the pCO_{2w} value of the neuron whose Chl-a, SST, SSS, SIC, xCO_{2a}, and X and

305 Y values were most similar to those of that grid-cell. If the most similar neuron was not

306 labeled with a pCO_{2w} value, then the pCO_{2w} value of the neuron that was most similar

307   *and* labeled was used. That case often happened in periods and regions without any

308   observed data. A detailed description of the procedure can be found in Telszewski et al.

309   (2009) and Nakaoka et al. (2013).

310

311   3.5. Calculation of air–sea CO_2 fluxes

312   We calculated monthly air–sea CO_2 flux (F) values from the pCO_{2w} values estimated in

313   Sect. 3.4 by using the bulk formula:

314

315        $F = kL(pCO_{2w} - pCO_{2a})$,   (2)

316

317   where k is the gas transfer velocity and L is the solubility of CO_2. The solubility of CO_2

318   (L) was calculated as a function of SST and SSS (Weiss, 1974). We converted the

319   interpolated NOAA marine boundary layer xCO_{2a} data (Sect. 2.2) to pCO_{2a} by using

320   monthly sea-level pressure data and the water-vapor saturation pressure calculated from

321   monthly SST and SSS (Murray, 1967).

322   The gas transfer velocity k was calculated by using the formula of Sweeney et al.

323   (2007):

324

325 $\quad k = 0.19 \ (Sc/660)^{-0.5} \langle W_{NCEP2}^2 \rangle$, $\hspace{6cm}$ (3)

326

327 where Sc is the Schmidt number of CO_2 in seawater at a given SST, calculated

328 according to Wanninkhof (2014), "$\langle \rangle$" denotes the monthly mean, and $\langle W_{NCEP2}^2 \rangle$ is

329 the monthly mean of the second moment of the NCEP2 6-hourly wind speed. The

330 coefficient 0.19, which is the global average of $0.27\langle W_{NCEP1}^2 \rangle / \langle W_{NCEP2}^2 \rangle$, is based on

331 the one determined by Sweeney et al. (2007) but optimized for NCEP2 winds, following

332 the same method as Schuster et al. (2013) and Wanninkhof et al. (2013).

333 $\quad$ The suppression of gas exchange by sea ice was accounted for by correcting the air–

334 sea CO_2 fluxes using the parameterization presented by Loose et al. (2009); the flux is

335 proportional to $(1\text{-SIC})^{0.4}$. Following Bates et al. (2006), in the regions with SIC > 99 %,

336 we used SIC = 99 % to allow for non-negligible rates of air–sea CO_2 exchange through

337 leads, fractures, and brine channels (Semiletov et al., 2004; Fransson et al., 2017). This

338 parameterization reduces the flux in fully ice covered waters (SIC > 99%) by 84%.

339

340 **4. Uncertainty**

341 4.1. Uncertainty in chlorophyll-a concentration data

342 $\quad$ Fig. 3 shows original and interpolated Chl-a for the year 2012 as an example. Overall,

343   the interpolated Chl-a data seems to fit well with the original data. Most interpolated

344   Chl-a data have low concentrations because of high SIC and lack of sunlight. The

345   average of the interpolated Chl-a values is 0.1 mg m^{-3}, and less than 5% of the

346   interpolated Chl-a values are >0.5 mg m^{-3} (cf. the average of the original Chl-a values is

347   1.1 mg m^{-3}, and 48% of the original Chl-a values are >0.5 mg m^{-3}). The previous

348   studies to estimate pCO_{2w} in high-latitudes assumed missing Chl-a as constant values

349   and ignored spatio-temporal variation of Chl-a (Landschutzer et al. 2013; Nakaoka et al.

350   2013). However, original Chl-a values in the ice-edge region are not small as captured

351   by Perrette et al. (2011), and those in the northernmost grids in winter, north of which

352   the original Chl-a values are missing, is far south of polar night region, since they are

353   missing not because of no sunlight but because of low-angles of sunlight (Fig. 3a).

354   Therefore, we believe interpolation is better than lowest constant values.

355   To validate our Chl-a interpolation, we repeated the interpolation after randomly

356   eliminating 10 % of the satellite Chl-a values. We then used the eliminated original

357   Chl-a data as independent data for the validation. Note that this comparison was done

358   where there were the original Chl-a data, i.e. the high Chl-a region. The root mean

359   square difference (RMSD) and correlation coefficient between the interpolated and the

360   independent original Chl-a data are 0.90 mg m^{-3} and 0.80, respectively. It means the

361 interpolated Chl-a, maybe not quantitatively, but qualitatively reproduced the original

362 Chl-a, and therefore is a meaningful parameter in the SOM process. Actually Chl-a data

363 improved the pCO_{2w} estimate, even though Chl-a values in many grid-cells were

364 interpolated values (see Sec. 5.4).

365   To evaluate our choice of Chl-a algorithm (i.e. the Arctic algorithm of Cota et al.,

366 2004), we compared its calculated Chl-a values with those determined by using the

367 standard algorithm of O'Reilly et al. (1998) and the coastal algorithm of Tassan (1994).

368 RMDS and correlation coefficient (r) between the original (i.e. non-interpolated) Chl-a

369 values are about 0.8 mg m^{-3} and 0.9, respectively (Table 1). For all the Chl-a values

370 including the interpolated data, they are about 0.4 mg m^{-3} and 0.9. The lower RMSD in

371 this case results from the fact that most of the interpolated Chl-a values have low

372 concentrations. This result means the Chl-a from the different algorisms, maybe not

373 quantitatively, but qualitatively consistent with each other. Since not absolute Chl-a

374 values but relative values affect the pCO_{2w} estimates in the SOM technique, the large

375 RMSD among the Chl-a does not result in the significant difference of the pCO_{2w}

376 estimates. Actually, the pCO_{2w} and CO_2 fluxes determined using Chl-a from any of

377 these algorithms as input to the SOM are consistent within their uncertainties (see Sects.

378 4.2 and 4.3 below). RMSDs between the observed and estimated pCO_{2w} are smallest in

379   pCO_{2w} estimate using Chl-a from the Arctic algorism, but the differences are quite small

380   (<1%).

381

382   4.2. Uncertainty of pCO_{2w} mapping

383   Fig. 4 compares observed and estimated pCO_{2w} (note that the spatial change visible in

384   Figs. 4a and 4b include differences generated by different seasonal coverage of data in

385   the various regions). Both observed and estimated pCO_{2w} tend to be higher in the

386   subpolar North Atlantic, the Laptev Sea, and the Canada Basin, and lower in the

387   Greenland Sea and the Barents Sea. However, the east–west contrast in the Bering Sea

388   and the contrast between the Canada Basin and the Chukchi Sea are weaker in our

389   estimates than in the observations, and mean bias and RMSD are relatively large in

390   those areas (Figs. 4c and 4d). The temporal changes in the observed and estimated

391   pCO_{2w} are in phase (Fig. 5a), although the variability of the estimated values is

392   somewhat suppressed compared to that of the observed data (Note that the temporal

393   change depicted in Fig. 5a also includes changes incurred by time variations in data

394   coverage). The mean bias and RMSD fluctuate seasonally but are at a constant level

395   over the years (Fig. 5b).

396   The correlation coefficient between estimated and observed pCO_{2w} is 0.82, and the

397 RMSD is 30 μatm, which is 9 % of the average and 58 % of the standard deviation of

398 the observed pCO_{2w} values. This is a performance level categorized as "good" by

399 Maréchal (2004). The differences between the estimated and observed values stem not

400 only from the estimation error but also from the error of the gridded observed data. The

401 uncertainty of the pCO_{2w} measurements is 2–5 μatm (Bakker et al., 2014), the

402 uncertainty of the pCO_{2w} values calculated from dissolved inorganic carbon and total

403 alkalinity, whose uncertainties are within 4 μmol kg^{-1} and 6 μmol kg^{-1}, respectively

404 (Olsen et al., 2016), can be up to 14 μatm (Lueker et al., 2000), and the sampling error

405 of the gridded pCO_{2w} observation data was determined from the standard errors of

406 monthly observed pCO_{2w} in the 1° × 1° grid-cells, to 7 μatm (Yasunaka et al., 2016).

407   To validate our estimated pCO_{2w} values for periods and regions without any observed

408 data, we repeated the mapping experiments after systematically excluding some of the

409 observed pCO_{2w} data when labeling the neurons; four experiments were carried out, by

410 excluding data (1) from 1997–2004, (2) from January to April, (3) from north of 80°N,

411 and (4) from the Laptev Sea (90°E – 150°E), where there are only a few pCO_{2w}

412 observations. We compared the pCO_{2w} estimates obtained in each experiment with the

413 excluded observations and found that the pCO_{2w} estimates reproduced the general

414 features of the excluded data, both spatially and temporally (not shown here). They

415 were also similar to the pCO_{2w} estimates obtained by using all observations, although

416 the RMSDs between the estimates and the excluded observations are 54 μatm on

417 average, which is 1.8 times the RMSDs of the estimates based on all observations. It

418 means that our estimated pCO_{2w} reproduce the general features both in space and time

419 even when and where there are no observed data, although the uncertainty in pCO_{2w}

420 might be as large as 54 μatm in regions and periods without data. We used this

421 uncertainty for pCO_{2w} estimates made by using the pCO_{2w} values of a less similar

422 neuron.

423

424 4.3. Uncertainty of CO_2 flux estimates

425 Signorini and McClain (2009) estimated the uncertainty of the CO_2 flux resulting from

426 uncertainties in the gas exchange parameterization to be 36 %, and that resulting from

427 uncertainties in the wind data to be 11 %. The uncertainty for SIC is 5 % (Cavalieri et

428 al., 1984; Gloersen et al., 1993; Peng et al., 2013). The standard error of the sea-ice

429 effect on gas exchange was estimated to about 30 % by Loose et al. (2009). The

430 uncertainty of pCO_{2a} is about 0.5 μatm

431 (http://www.esrl.noaa.gov/gmd/ccgg/mbl/mbl.html), and that of pCO_{2w} was 30 μatm

432 (Sect. 4.2); therefore, we estimated the uncertainty of ΔpCO_2 ($=pCO_{2w} - pCO_{2a}$) to be

433 34 % (average $\Delta p\mathrm{CO_2}$ in the analysis domain and period was -89 µatm). The overall

434 uncertainty of the estimated $\mathrm{CO_2}$ fluxes is thus 59 % ($[0.36^2 + 0.11^2 + 0.05^2 + 0.3^2 +$

435 $0.34^2]^{1/2}$) in sea-ice covered regions and 51 % ($[0.36^2 + 0.11^2 + 0.34^2]^{1/2}$) in ice-free

436 regions. For estimates using the $p\mathrm{CO_{2w}}$ values of a less similar neuron, whose

437 uncertainty in $p\mathrm{CO_{2w}}$ is 54 µatm and the uncertainty of the $\Delta p\mathrm{CO_2}$ estimates can be as

438 high as 61 %, the uncertainty is 78 % ($[0.36^2 + 0.11^2 + 0.05^2 + 0.3^2 + 0.61^2]^{1/2}$) in

439 sea-ice covered regions, and 72 % ($[0.36^2 + 0.11^2 + 0.61^2]^{1/2}$) in ice-free regions. The

440 average of the estimated $\mathrm{CO_2}$ flux in the analysis domain and period is 4.8 mmol m^{-2} d^{-}

441 ^{1}; hence the uncertainty of the $\mathrm{CO_2}$ flux estimate corresponds to 2.8 mmol m^{-2} d^{-1} in

442 sea-ice covered regions and 2.4 mmol m^{-2} d^{-1} in ice-free regions. For estimates using

443 the $p\mathrm{CO_{2w}}$ values of a less similar neuron, the uncertainty corresponds to 3.7 mmol m^{-2}

444 d^{-1} in the sea-ice covered region and 3.5 mmol m^{-2} d^{-1} in ice-free regions.

445

446 **5. Results and discussion**

447 5.1. Relationship between $p\mathrm{CO_2}$ and chlorophyll-a

448 Fig. 6 compares the observed $p\mathrm{CO_{2w}}$ and the original non-interpolated Chl-a in spring

449 (March–May) and summer (July–September). In spring, when much of the Arctic Ocean

450 is ice-covered, Chl-a is high in the Barents Sea and the Bering Strait (>1 mg m^{-3}). In

451 summer, when the ice cover is less extensive, Chl-a is high in the Chukchi Sea, the Kara

452 Sea, the Laptev Sea, and the East Siberian Sea (>1 mg m^{-3}) and especially high in the

453 coastal regions of the two latter (>2 mg m^{-3}). pCO$_{2w}$ is high in the Norwegian Sea in

454 spring, and in the Kara Sea, the Laptev Sea and the Canada Basin during summer (>300

455 µatm). On the other hand, it is lower in the Chukchi Sea, Bering Strait area and the

456 sea-ice edge region of the Eurasian Basin in summer (<300 µatm). The overall

457 correlation between pCO$_{2w}$ and Chl-a is negative where Chl-a ≤ 1 mg m^{-3} (70% of all

458 the data; correlation coefficient $r = -0.36$, $P < 0.01$), but there is no significant

459 relationship where Chl-a > 1 mg m^{-3} (Fig. 7). A similar situation was identified in the

460 subpolar North Atlantic by Olsen et al. (2008). It means that primary production

461 generally draws down the pCO$_{2w}$, but high Chl-a are not necessarily associated with the

462 low pCO$_{2w}$ probably because high Chl-a usually appears in the coastal regions (Fig. 6b;

463 see below).

464 To determine the spatial variability of the relationship between pCO$_{2w}$ and Chl-a, we

465 calculated the correlation coefficients between pCO$_{2w}$ and Chl-a in a window of $\pm5°$ of

466 latitude, and $\pm30°$ of longitude for each monthly $1° \times 1°$ grid-cell (Fig. 8a). The

467 correlations between pCO$_{2w}$ and Chl-a are negative in the Greenland/Norwegian Seas

468 and over the Canada Basin. In the Greenland/Norwegian Seas, the correlation between

469    $p\mathrm{CO}_{2w}$ and Chl-a is strongly negative ($r < -0.4$) in spring and weakly negative ($-0.4 < r$

470   < 0) in summer. Chl-a there is higher in summer than in spring (Fig. 6b), whereas

471   nutrient concentrations are high in spring and low in summer (Fig. 8b). Taken together,

472   this suggest that primary production draws down the $p\mathrm{CO}_{2w}$ in spring, whereas in

473   summer the primary production mostly depends on regenerated nutrients (Harrison and

474   Cota, 1991) and the net CO_2 consumption is small, as also reported for the subpolar

475   North Atlantic (Olsen et al., 2008). Therefore the correlation between $p\mathrm{CO}_{2w}$ and Chl-a

476   becomes less negative. In the eastern Barents Sea, the Kara Sea and the East Siberian

477   Sea, and the Bering Strait, the correlations are positive because of water with high

478    $p\mathrm{CO}_{2w}$ and Chl-a in the coastal region subjected to river discharge (Murata, 2006;

479   Semiletov et al., 2007; Anderson et al., 2009; Manizza et al., 2011). In the Chukchi Sea,

480   the relationship is weak ($-0.2 < r < 0.2$), probably because the relationship is on smaller

481   spatial and temporal scales than those represented by the window size used here, as

482   shown by Mucci et al. (2010). The occurrence of calcifying plankton blooms in this

483   region, likely also weakens the correlation since the calcification increases $p\mathrm{CO}_{2w}$

484   (Shutler et al., 2013; Fransson et al., 2017).

485   These results show that $p\mathrm{CO}_{2w}$ relates Chl-a, but the relationships are different

486   depending on the region and the season. It is difficult to represent such a complex

487   relationship using simple equations (e.g. multiple regression methods) because it needs

488   a priori assumptions of regression functions and of dividing the basin into sub-regions.

489   But the SOM technique can empirically induce the relationships without any of the a

490   priori assumptions, and therefore is suitable to represent such a complex relationship.

491

492   5.2. Spatiotemporal CO_2 flux variability

493   The 18-year annual mean CO_2 flux distribution shows that all areas of the Arctic

494   Ocean and its adjacent seas were net CO_2 sinks over the time period that we

495   investigated (Fig. 9). The annual CO_2 influx to the ocean was strong in the

496   Greenland/Norwegian Seas (9 ± 3 mmol m^{-2} d^{-1}; 18-year annual mean $\pm$ uncertainty

497   averaged over the area shown in Fig. 1), the Barents Sea (10 ± 3 mmol m^{-2} d^{-1}), and the

498   Chukchi Sea (5 ± 3 mmol m^{-2} d^{-1}). In contrast, influx was weak and not statistically

499   significantly different from zero in the Eurasian Basin, the Canada Basin, the Laptev

500   Sea and the East Siberian Sea. Our annual CO_2 flux estimates are consistent with those

501   reported by Yasunaka et al. (2016) and other previous studies (Bates and Mathis, 2009,

502   and references therein).

503   The estimated 18-year average CO_2 influx to the Arctic Ocean was 5 ± 3 mmol m^{-2} d^{-}

504   ^{1}, equivalent to an uptake of 180 ± 130 TgC y^{-1} for the ocean area north of 65° N,

505   excluding the Greenland/Norwegian Seas and Baffin Bay (10.7×10^6 km^2; see Fig. 1).

506   This accounts for 12% of the net global CO_2 uptake by the ocean of 1.5 PgC yr^{-1}

507   (Gruber et al., 2009; Wanninkhof et al., 2013; Landschützer et al., 2014). It is within the

508   range of other estimates (81–199 TgC y^{-1}; Bates and Mathis, 2009), but close to the

509   upper bound. That is partly because the parameterization of the suppression effect by

510   sea ice used in this study. Using another parameterization which represents the SIC

511   effect linearly (Takahashi et al. 2009; Butterworth and Miller 2016), CO_2 uptake of the

512   Arctic Ocean was estimated to be 130 ± 110 TgC y^{-1}.

513   Fig. 10 shows the seasonal variation of the air-sea CO_2 fluxes and its controlling

514   factors ($\Delta p CO_2$, wind speed and SIC; solubility is not shown as the impacts of its

515   variations are relatively small in this context) in the Greenland/Norwegian Seas, the

516   Barents Sea, the Chukchi Sea and the Arctic Ocean. In all of these regions the influxes

517   are strongest in October, when the winds strengthen with the approach of winter and the

518     $p CO_{2w}$ and/or SIC are still as low as in the summer. In the Greenland/Norwegian Seas

519   and the Barents Sea the CO_2 influx shows a secondary maximum in February because

520   the strongest winds occur in that month, while in the Chukchi Sea and Arctic Ocean, the

521   winds are also strong but the flux is suppressed by the extensive sea-ice cover. All of

522   these regions are undersaturated with $p CO_{2w}$ (i.e. negative $\Delta p CO_2$) throughout all

523   seasons. The undersaturation is strongest in the Arctic Ocean, as this has the most

524   extensive sea ice cover limiting the fluxes from the atmosphere and the strongest

525   stratification, limiting the mixing of CO_2 rich subsurface waters into the surface ocean.

526   The undersaturation typically shows a maximum (i.e. ΔpCO_2 is minimum) in late spring

527   to early summer (May–June) when the spring bloom occur (Pabi et al. 2008), but not in

528   the Arctic Ocean. Here the undersaturation reaches its minimum (ΔpCO_2 is the smallest)

529   in late summer (August–September) at the time of minimum sea ice cover, since the

530   seasonal decrease of pCO_2 in summer is larger in the air than in the sea. Overall, in the

531   Greenland/Norwegian Seas and the Barents Sea the seasonal variations of the CO_2 flux

532   is opposite to that expected from the seasonal ΔpCO_2 variations because it is the wind

533   speed that governs most of the seasonal flux variations. In the Chukchi Sea, on the other

534   hand, the CO_2 influx is strongest in summer, a consequence of the minimum sea-ice

535   cover and strongest pCO_2 undersaturation. In the Arctic Ocean it is the SIC and wind

536   speed that drive the seasonal flux variations. Seasonal variations of CO_2 flux are

537   consistent with those of the previous studies (Yasunaka et al. 2016, and references

538   therein), whereas those of pCO_{2w} become realistic (see Section 5.3 below).

539   Fig. 11 shows interannual variation of CO_2 flux and its driving factors in these four

540   regions. The interannual variations of CO_2 flux and ΔpCO_2 are generally smaller than

541   the seasonal variations, and are often smaller than their respective uncertainty. In the

542   Greenland/Norwegian Sea, interannual variation of the CO_2 flux negatively correlates

543   with the wind speed (CO_2 influx to the ocean is large when the wind is strong; r = −

544   0.41), while interannual variation of ΔpCO_2 and sea ice change is small. In the Barents

545   Sea, the interannual variation of CO_2 flux correlates with ΔpCO_2 positively (r = 0.71)

546   and with SIC negatively (r = −0.50), while the correlation with wind speed is not

547   significant. Although low SIC enhance the air-sea CO_2 exchange due to increase of the

548   area of open water, it also associates with high SST and therefore high pCO_{2w} there. In

549   the Chukchi Sea, CO_2 influx to ocean is decreasing with the increasing of ΔpCO_2 (r =

550   0.87). High pCO_{2w} (>500 μatm) via storm-induced deep mixing events has been

551   sometimes observed in the Chukchi Sea after 2010 (Hauri et al. 2013; Taro Takahashi,

552   personal communication). Interannual variability of the CO_2 flux averaged over the

553   Arctic Ocean is small because the increasing ΔpCO_2 is compensated by the effect of sea

554   ice retreat (r = −0.70). Thus, the combined effect of sea-ice retreat and pCO_{2w} increase

555   on CO_2 flux varied among regions.

556   The CO_2 influx has been increasing in the Greenland Sea and northern Barents Sea,

557   and decreasing in the Chukchi Sea and southern Barents Sea (Fig. 12). The CO_2 flux

558   trend corresponds well with the ΔpCO_2 trend, which in turn corresponds well with the

559   SST trend. The increasing CO_2 influx in the northern Barents Sea also corresponds with

560   the sea-ice retreat. These results are similar to that for the previous estimates without

561   using Chl-a (see Fig. 10 in Yasunaka et al., 2016). It shows again that the combined

562   effect of sea-ice retreat and pCO_{2w} increase to the CO_2 flux is regionally different. In the

563   SOM process, the pCO_{2w} values observed in the latter period might be used for the

564   pCO_{2w} estimate in the former period where the pCO_{2w} measurements have not been

565   made, and therefore the trend in CO_2 influx might be affected by the spatio-temporal

566   distribution of the measurements. To confirm this is not the case, we checked that the

567   spatial distribution of the pCO_{2w} trend did not correspond to the year when the first

568   observation was conducted (see supplement).

569

570   5.3. Impact of incorporating chlorophyll-a data in the SOM

571   To determine the impact of including Chl-a data in the SOM process, the analyses were

572   repeated without Chl-a data. The RMSD of the resulting estimated pCO_{2w} values is 33

573   μatm, which is 3 μatm larger than the uncertainty of the estimates generated by

574   including Chl-a in the SOM. Chl-a data thus improved the pCO_{2w} estimate (namely, a

575   10 % reduction of RMSD), even though 40 % of the Chl-a data labeled with pCO_{2w}

576   observations were interpolated Chl-a values.

577   Figs. S1 and S2 present the difference in bias and RMSD for pCO_{2w} estimated with

578   and without Chl-a; Fig. S1 shows the time-evolution and Fig. S2 shows the spatial

579   distribution. Both approaches typically underestimate pCO_{2w} in winter and overestimate

580   the summertime values, but these systematic biases are reduced when Chl-a are

581   included in the SOM (Fig. S1). Biases and RMSDs are reduced in the Canada basin, the

582   western Bering Sea, and the boundary region between the Norwegian Sea and the

583   subpolar North Atlantic (Fig. S2). As a result the strong east–west contrast in the Bering

584   Sea and the contrast between the Canada Basin and the Chukchi Sea (see Fig. 4) are

585   better represented when Chl-a is included. Taken together, inclusion of Chl-a when

586   estimating pCO_{2w} yields not only better representation of the pCO_{2w} decline in spring

587   and summer but also improves the representation of the spatio-temporal pCO_{2w}

588   distribution. Technically, these improvements come from the fact that Chl-a as a training

589   parameter can separate high Chl-a region/time and low Chl-a region/time into different

590   neurons, which contaminated in the same neurons trained without Chl-a. For example,

591   since Chl-a is high in spring but SST and SIC are still in the similar levels with winter,

592   the grid-cells in spring and winter would be classified into the separate neurons when

593   Chl-a is included as a training parameter, but in the same neuron when Chl-a is not

594   included. As a result, without Chl-a, the estimated pCO_{2w} in spring tends to be similar to

595 the pCO_{2w} in winter, and the pCO_{2w} in winter tends to be similar to that in spring. And

596 therefore the contrast between winter and spring is weakened without Chl-a.

597   The seasonal cycles of pCO_{2w} estimates derived with the inclusion of Chl-a have a

598 larger amplitude than the uncertainties, whereas the uncertainties are larger than the

599 seasonal amplitude when pCO_{2w} is derived without Chl-a (upper panels of Fig. 13). The

600 difference is caused by the fact that the seasonal cycle of pCO_{2w} in each region

601 reproduces the observed cycle better when Chl-a was included (lower panels of Fig. 13).

602 Note that the much larger seasonal amplitude in the lower panels is an artefact generated

603 by the seasonal bias in sampling locations; in winter most measurements are obtained at

604 low latitudes where pCO_{2w} is typically higher than at high latitudes.

605   Compared to the CO_2 influx estimates by Yasunaka et al. (2016), the winter CO_2

606 influx in the Greenland/Norwegian Seas estimated including Chl-a is about 3 mmol m^{-2}

607 d^{-1} less than that calculated without using Chl-a (Fig. 14), but this difference is smaller

608 than the uncertainties. The CO_2 fluxes in the other area are quite similar with each

609 estimate, while their uncertainties are smaller in the present estimates.

610   The inclusion of Chl-a data also reduced the uncertainty of the estimated annual

611 air-sea CO_2 flux integrated over the entire Arctic Ocean. Compared to the flux estimate

612 determined by Yasunaka et al. (2016) of 180 ± 210 TgC y^{-1}, the CO_2 uptake in the

613 Arctic Ocean estimated here is significant within its uncertainty (180 ± 130 TgC y^{-1}).

614 This improvement is the result of 1) the inclusion of Chl-a data in the SOM process

615 (which reduced the uncertainty by 23 %); 2) the separate uncertainty estimates for

616 ice-free and ice-covered regions (8 %); and 3) the addition of new observational pCO$_{2w}$

617 data (7 %). Reducing the uncertainty of this quantification is a key contribution to the

618 larger work of constraining the global carbon budget (e.g., Le Quere et al., 2016).

619 Because the Arctic is an important CO$_2$ sink, quantifying its fluxes and minimizing the

620 uncertainty is of great scientific value.

621

622 5.4. Toward further reduction of the uncertainty

623   The addition of new observational data from SOCATv4 and GLODAPv2 reduced the

624 overall uncertainty in the mapped pCO$_{2w}$: a 33 % increase in the number of observations

625 induced a 7 % reduction in the uncertainty. However, there are still few observations in

626 the Kara Sea, the Laptev Sea, the East Siberian Sea and the Eurasian Basin (Fig. 2). To

627 improve our understanding of the variability in air–sea CO$_2$ fluxes in the Arctic, it is of

628 critical importance to obtain additional ocean CO$_2$ measurements to fill these data gaps,

629 and that these measurements are made publically available. Data synthesis activities like

630 SOCAT must be encouraged.

631   In the present study, we discussed the combined effect of sea-ice retreat and pCO_{2w}

632   change on the air-sea CO_2 flux. There are other factors that will induce the change of

633   CO_2 flux. For example, warmer temperature will lead to an increasing buffering

634   capacity while lower salinity will have the opposite effect and cause a decrease in

635   buffering capacity. In our current study, we used climatological-mean salinity for the

636   pCO_{2w} estimate because of lack of reliable year-to-year salinity data. That might be one

637   of the improvements for a future study.

638

639   **6. Conclusions**

640   By applying an SOM technique with the inclusion of Chl-a data to estimate pCO_{2w}, we

641   produced monthly maps of air–sea CO_2 fluxes from 1997 to 2014 for the Arctic Ocean

642   and its adjacent seas north of 60° N. Negative correlation between pCO_{2w} and Chl-a

643   meant that Chl-a is valuable parameter to represent primary production. Since the

644   relationship varied among seasons and regions, the SOM technique is better suited for

645   the mapping than a multiple linear regression approach. Adding Chl-a to the SOM

646   process improved representation of the seasonal cycle of pCO_{2w}, and therefore reduced

647   the uncertainty of the CO_2 flux estimates.

648   In the Greenland/Norwegian Seas and the Barents Sea the CO_2 influx was large in

649   autumn and winter because of the strong wind. In the Chukchi Sea, on the other hand,

650   the CO_2 influx was strong in summer and autumn, as a consequence of the low SIC and

651   strong pCO_{2w} undersaturation. Although interannual variation of the CO_2 influx was

652   smaller than the seasonal variation, the CO_2 influx has been increasing in the Greenland

653   Sea and northern Barents Sea, and decreasing in the Chukchi Sea and southern Barents

654   Sea.

655   A major goal of the carbon-cycle research community in recent years has been to

656   reduce the uncertainty in estimates of carbon reservoirs and fluxes. Our results

657   contribute to this in that CO_2 uptake in the Arctic Ocean is demonstrated with high

658   significance. The resulting estimate of the annual Arctic Ocean CO_2 uptake of 180 TgC

659   y^{-1} is significant with an uncertainty of $\pm$ 130 TgC y^{-1}. This is a substantial

660   improvement over earlier estimates, and is due mainly to the incorporation of Chl-a

661   data.

662   Assessment of the numerical models using our estimate of Arctic carbon uptake is

663   also an interesting topic since numerical models are poorly validated in the Arctic due to

664   the limited observations of biogeochemistry (Popova et al., 2012). However, such

665   experiments need thorough insight into the numerical models, which is beyond the

666   scope of this study. We hope to perform such comparisons in future studies.

667   The monthly CO_2 flux, pCO_{2w}, and interpolated Chl-a data presented in this paper

668   will be available at the JAMSTEC website

669   (http://www.jamstec.go.jp/res/ress/yasunaka/co2flux_v2).

670

671   **Acknowledgments**

672   We thank the many researchers and funding agencies responsible for the collection of

673   data and quality control for their contributions to SOCAT and GLODAPv2. We are

674   grateful for the use of the CO2SYS program obtained from the Ocean Carbon Data

675   System   of   NOAA   National   Centers   for   Environmental   Information

676   (https://www.nodc.noaa.gov/ocads/oceans/CO2SYS/co2rprt.html), and SOM Toolbox

677   Version 2 developed by the Laboratory of Information and Computer Science at

678   Helsinki University of Technology (http://www.cis.hut.fi/projects/somtoolbox). We

679   thank ACRI-ST, France, for developing, validating, and distributing the GlobColour

680   data used in this work. This work was financially supported by the Arctic Challenge for

681   Sustainability (ArCS) Project funded by the Ministry of Education, Culture, Sports,

682   Science and Technology, Japan. Are Olsen was supported by grants from the Norwegian

683   Research Council (Subpolar North Atlantic Climate States [SNACS] 229752 and the

684   Norwegian component of the Integrated Carbon Observation System [ICOS-Norway]

245927). Mario Hoppema was partly supported by the German Federal Ministry of

Education and Research (grant no. 01LK1224I; ICOS-D). Siv K. Lauvset acknowledges

support from the Norwegian Research Council (VENTILATE, 229791) and the EU

H2020 project AtlantOS (grant agreement no. 633211). Rik Wanninkhof and Taro

Takahashi acknowledge support from the Office of Oceanic and Atmospheric Research

(OAR) of the United States NOAA, including resources from the Ocean Observation

and Monitoring Division of the Climate Program Office (fund reference100007298).

References

Anderson, L. G., Jutterström, S., Hjalmarsson, S., Wåhlström, I., and Semiletov, I. P.:
Out-gassing of CO_2 from Siberian Shelf seas by terrestrial organic matter
decomposition, Geophys. Res. Lett., 36, L20601, doi:10.1029/2009GL040046, 2009.

Ardyna, M., Babin, M., Gosselin, M., Devred, E., Rainville, L., and Tremblay, J.-É.:
Recent Arctic Ocean sea ice loss triggers novel fall phytoplankton blooms, Geophys.
Res. Lett., 41, 6207–6212, doi:10.1002/2014GL061047, 2014.

Arrigo, K. R., and van Dijken, G. L.: Annual cycles of sea ice and phytoplankton near
Cape Bathurst, southeastern Beaufort Sea, Canadian Arctic, Geophys. Res. Lett., 31,
L08304, doi:10.1029/2003GL018978, 2004.

703   Assmy P. M. Fernandez-Mendez, Duarte, P., Meyer, A., Randelhoff, A., Mundy, C. J.,

704   Olsen, L. M., Kauko, H. M., Bailey, A., Chierici, M., Cohen, L., Doulgeris, A. P.,

705   Ehn, J. K., Fransson, A., Gerland, S., Hop, H., Hudson, S. R., Hughes, N., Itkin, P. ,

706   Johnsen, G. , King, J. A., Koch, B. P. , Koenig, Z., Kwasniewski, S., Laney, S. R.,

707   Nicolaus, M., Pavlov, A. K., Polashenski, C. M., Provost, C., Rösel, A., Sandbu, M.,

708   Spreen, G., Smedsrud, L. H., Sundfjord, A., Taskjelle, T., Tatarek, A., Wiktor, J.,

709   Wagner, P. M., Wold, A., Steen, H., and Granskog, M. A.: Leads in Arctic pack ice

710   enable early phytoplankton blooms below snow-covered sea ice. Scientific Report,

711   7:40850, DOI: 10.1038/srep40850, 2017.

712   Bakker, D. C. E., Pfeil, B., Smith, K., Hankin, Olsen, A., Alin, C. Cosca, S. R.,

713   Harasawa, S., Kozyr, A., Nojiri, Y., O'Brien, K. M., Schuster, U., Telszewski, M.,

714   Tilbrook, B., Wada, C., Akl, J., Barbero, L., Bates, N., Boutin, J., Cai, W.-J., Castle,

715   R. D., Chavez, F. P., Chen, L., Chierici, M., Currie, K., de Baar, H. J. W., Evans, W.,

716   Feely, R. A., Fransson, A., Gao, Z., Hales, B., Hardman-Mountford, N., Hoppema,

717   M., Huang, W.-J., Hunt, C. W., Huss, B., Ichikawa, T., Johannessen, T., Jones, E. M.,

718   Jones, S., Jutterstrøm, S., Kitidis, V., Körtzinger, A., Lauvset, S. K., Lefèvre, N.,

719   Manke, A. B., Mathis, J. T., Merlivat, L., Metzl, N., Murata, A., Newberger, T., Ono,

720   T., Park, G.-H., Paterson, K., Pierrot, D., Ríos, A. F., Sabine, C. L., Saito, S.,

721   Salisbury, J., Sarma, V. V. S. S., Schlitzer, R., Sieger, R., Skjelvan, I., Steinhoff, T.,

722   Sullivan, K., Sun, H., Sutton, A. J., Suzuki, T., Sweeney, C., Takahashi, T., Tjiputra,

723   J., Tsurushima, N., van Heuven, S. M. A. C., Vandemark, D., Vlahos, P., Wallace, D.

724   W. R., Wanninkhof, R., and Watson, A. J.: An update to the Surface Ocean CO_2 atlas

725   (SOCAT version 2). Earth System Science Data, 6, 69–90,

726   doi:10.5194/essd-6-69-2014, 2014.

727 Bakker, D. C. E., Pfeil, B., Smith, K., Harasawa, S., Landa, C., Nakaoka, S., Nojiri, Y.,

728   Metzl, N., O'Brien, K. M., Olsen, A., Schuster, U., Tilbrook, B., Wanninkhof, R.,

729   Alin, S. R., Barbero, L., Bates, N. R., Bianchi, A. A., Bonou, F., Boutin, J., Bozec, Y.,

730   Burger, E., Cai, W.-J., Castle, R. D., Chen, L., Chierici, M., Cosca, C., Currie, K.,

731   Evans, W., Featherstone, C., Feely, R. A., Fransson, A., Greenwood, N., Gregor, L.,

732   Hankin, S., Hardman-Mountford, N. J., Harlay, J., Hauck, J., Hoppema, M., Humpt,

733   L., Monteiro, P., Munro, D., Murata, A., Newberger, T., Omar, A. M., Ono, T.,

734   Paterson, K., Pierrot, D., Robbins, L. L., Sabine, C. L., Saito, S., Salisbury, J.,

735   Schneider, B., Schlitzer, R., Sieger, R., Skjelvan, I., Steinhoff, T., Sullivan, K. F., St,

736   L., Monteiro, P., Munro, D., Murata, A., Newberger, T., Omar, A. M., Ono, T.,

737   Paterson, K., Pierrot, D., Robbins, L. L., Sabine, C. L., Saito, S., Salisbury, J.,

738   Schneider, B., Schlitzer, R., Sieger, R., Skjelvan, I., Steinhoff, T., Sullivan, K. F.,

739   Sutherland, S. C., Sutton, A. J., Sweeney, C., Tadokoro, K., Takahashi, T., Telszewski,

740   M., Van Heuven, S. M. A. C., Vandemark, D., Wada, C., Ward, B., and Watson, A. J.:

741   A multi-decade record of high quality fCO_2 data in version 3 of the Surface Ocean

742   CO_2 Atlas (SOCAT). Earth System Science Data, 8, 383–413.

743   doi:10.5194/essd-8-383-2016, 2016.

744   Bates, N. R., and Mathis, J. T.: The Arctic Ocean marine carbon cycle: evaluation of

745   air-sea CO_2 exchanges, ocean acidification impacts and potential feedbacks,

746   Biogeosciences, 6, 2433-2459, doi:10.5194/bg-6-2433-2009, 2009.

747   Bates, N. R., Moran, S. B., Hansell, D. A., and Mathis, J. T.: An increasing CO_2 sink in

748   the Arctic Ocean due to sea-ice loss, Geophys. Res. Lett., 33, L23609,

749   doi:10.1029/2006GL027028, 2006.

750   Bates, N. R., Garley, R., Frey, K. E., Shake, K. L., and Mathis J. T.: Sea-ice melt

751   CO_2-carbonate chemistry in the western Arctic Ocean: meltwater contributions to

752   air-sea CO_2 gas exchange, mixed layer properties and rates of net community

753   production under sea ice. Biogeosciences, 11, 6769–6789,

754   doi:10.5194/bg-11-6769-2014., 2014

755   Boyer, T. P., Antonov, J. I., Baranova, O. K., Coleman, C., Garcia, H. E., Grodsky, A.,

756   Johnson, D. R., Locarnini, R. A., Mishonov, A. V., O'Brien, T. D., Paver, C. R.,

757   Reagan, J. R., Seidov, D., Smolyar, I. V., and Zweng, M. M.: World Ocean Database

758   2013. Sydney Levitus, Ed.; Alexey Mishonov, Technical Ed.; NOAA Atlas NESDIS

759   72, 209 pp, 2013.

760   Butterworth, B. J., and Miller, S. D.: Air-sea exchange of carbon dioxide in the Southern

761   Ocean and Antarctic marginal ice zone. Geophys. Res. Lett., 43, 7223–7230,

762   doi:10.1002/2016GL069581, 2016.

763   Cai, W.J., Chen, L. Q., Chen, B. S., Gao, Z. Y., Lee, S. H., Chen, J. F., Pierrot, D.,

764   Sullivan, K., Wang, Y.C., Hu, X. P., Huang, W. J., Zhang, Y. H., Xu, S. Q., Murata, A.,

765   Grebmeier, J. M., Jones, E. P., and Zhang, H. S.: Decrease in the CO_2 uptake capacity

766   in an ice-free Arctic Ocean Basin. Science, 329, 556–559,

767   doi:10.1126/science.1189338, 2010.

768   Cavalieri, D. J., Gloersen, P., and Campbell, W. J.: Determination of sea ice parameters

769   with the NIMBUS-7 SMMR, J. Geophys. Res., 89, 5355–5369, 1984.

770   Chierici, M., Olsen, A., Johannessen, T., Trinañes, J., Wanninkhof, R.: Algorithms to

771   estimate CO_2 in the northern North Atlantic using observations, satellite and ocean

772   analysis data, Deep-Sea Res. II, 56, 630–639, doi:10.1016/j.dsr2.2008.12.01, 2009.

773   Chierici, M, Fransson, A., Lansard, B., Miller, L. A., Mucci, A., Shadwick, E., Thomas,

774   H., Tremblay, J.-E., and Papakyriakou, T.: The impact of biogeochemical processes

775   and environmental factors on the calcium carbonate saturation state in the

776   Circumpolar Flaw Lead in the Amundsen Gulf, Arctic Ocean. J. Geophys. Res., 116,

777   C00G09, doi:10.1029/2011JC007184, 2011.

778   Conway, T.J., Tans, P. P., Waterman, L. S., Thoning, K. W., Kitzis, D. R., Masarie, K. A.,

779   and Zhang, N.: Evidence for interannual variability of the carbon cycle from the

780   NOAA/CMDL global air sampling network. J. Geophys. Res., 99, 22831–22855,

781   1994.

782   Cota, G. F., Wang, J., and Comiso, J. C.: Transformation of global satellite chlorophyll

783   retrievals with a regionally tuned algorithm, Remote Sens. Environ. 89, 326–350,

784   doi:10.1016/j.rse.2004.01.005, 2004.

785   Dickson, A. G.: Standard potential of the reaction: $AgCl(s) + 1/2H_2(g) = Ag(s) +$

786    $HCl(aq)$, and the standard acidity constant of the ion HSO_4^- in synthetic seawater

787   from 273.15 to 318.15 K. J. Chemical Thermodynamics, 22, 113–127, 1990.

788   Else, B. G. T., Galley, R. J., Lansard, B., Barber, D. G., Brown, K., Miller, L. A., Mucci,

789   A., Papakyriakou, T. N., Tremblay, J.-É., and Rysgaard, S.: Further observations of a

790   decreasing atmospheric CO_2 uptake capacity in the Canada Basin (Arctic Ocean) due

791   to sea ice loss, Geophys. Res. Lett., 40, 1132–1137, doi:10.1002/grl.50268, 2013.

792   Fransson, A., Chierici, M., Skjelvan, I., Olsen, A., Assmy, P., Peterson, A. K., Spreen, G.,

793   and Ward, B.: Effects of sea-ice and biogeochemical processes and storms on

794   under-ice water fCO$_2$ during the winter-spring transition in the high Arctic Ocean:

795   Implications for sea-air CO$_2$ fluxes. J. Geophys. Res., doi:10.1002/2016JC012478,

796   2017.

797 Gao, Z., Chen, L., Sun, H., Chen, B., and Cai, W.-J.: Distributions and air–sea fluxes of

798   carbon dioxide in the Western Arctic Ocean, Deep-Sea Res. II, 81–84, 46–52,

799   doi:10.1016/j.dsr2.2012.08.021, 2012.

800 Gloersen, P., Campbell, W. J., Cavalieri, D. J., Comiso, J. C., Parkinson, C. L., and

801   Zwally, H. J.: Arctic and Antarctic sea ice, 1978–1987: Satellite passive-microwave

802   observations and analysis, NASA Spec. Publ., 511, 290 pp, 1993.

803 Gosselin, M., Levasseur, M., Wheeler, P. A., Horner, R. A., and B. C. Booth: New

804   measurements of phytoplankton and ice algal production in the Arctic Ocean,

805   Deep-Sea Res. II, 44, 1623–1644, doi:10.1016/S0967-0645(97)00054-4, 1997.

806 Harrison, W. G., and Cota., G. F.: Primary production in polar waters: relation to

807   nutrient availability, Polar Research, 10, 87–104,

808   doi:10.1111/j.1751-8369.1991.tb00637.x, 1991.

809 Hauri, C., Winsor, P., Juranek, L. W., McDonell, A. M. P., Takahashi, T. and Mathis, J.

810   T.: Wind-driven mixing causes a reduction in the strength of the continental shelf

811   carbon pump in the Chukchi Sea, Geophys. Res. Letters, 40, 5932-5936,

812   doi:10.1002/2013GL058267, 2013.

813   Iida, T., Saitoh, S. I., Miyamura, T., Toratani, M., Fukushima, H., and Shiga, N.:

814   Temporal and spatial variability of coccolithophore blooms in the eastern Bering Sea,

815   1998-2001, Prog. Oceanogr., 55, 165–175, 2002.

816   Kalnay, E., Kanamitsu, M., Kistler, R., Collins, W., Deaven, D., Gandin, L., Iredell, M.,

817   Saha, S., White, G., Woollen, J., Zhu, Y., Chelliah, M., Ebisuzaki, W., Higgins, W.,

818   Janowiak, J., Mo, K. C., Ropelewski, C., Wang, J., Leetmaa, A., Reynolds, R., Jenne,

819   R., and Joseph, D., The NCEP/NCAR 40-Year Reanalysis Project". Bull. Amer.

820   Meteor. Soc., 77, 437–471, 1996.

821   Kanamitsu, M., Ebisuzaki, W., Woollen, J., Yang, S-K, Hnilo, J. J., Fiorino, M., and

822   Potter, G. L., NCEP-DOE AMIP-II Reanalysis (R-2), Bull. Amer. Meteor. Soc., 83,

823   1631–1643, 2002.

824   Key, R.M., Olsen, A., van Heuven, S., Lauvset, S. K., Velo, A., Lin, X., Schirnick, C.,

825   Kozyr, A., Tanhua, T., Hoppema, M., Jutterström, S., Steinfeldt, R., Jeansson, E.,

826   Ishii, M., Perez, F. F., and T. Suzuki: Global Ocean Data Analysis Project, Version 2

827   (GLODAPv2), ORNL/CDIAC-162, ND-P093. Carbon Dioxide Information Analysis

828   Center, Oak Ridge National Laboratory, US Department of Energy, Oak Ridge,

829   Tennessee. doi: 10.3334/CDIAC/OTG.NDP093_GLODAPv2, 2015.

830   Le Quéré, C., Andrew, R. M., Canadell, J. G., Sitch, S., Korsbakken, J. I., Peters, G. P.,

831   Manning, A. C., Boden, T. A., Tans, P. P., Houghton, R. A., Keeling, R. F., Alin, S.,

832   Andrews, O. D., Anthoni, P., Barbero, L., Bopp, L., Chevallier, F., Chini, L. P., Ciais,

833   P., Currie, K., Delire, C., Doney, S. C., Friedlingstein, P., Gkritzalis, T., Harris, I.,

834   Hauck, J., Haverd, V., Hoppema, M., Klein Goldewijk, K., Jain, A. K., Kato, E.,

835   Körtzinger, A., Landschützer, P., Lefèvre, N., Lenton, A., Lienert, S., Lombardozzi,

836   D., Melton, J. R., Metzl, N., Millero, F., Monteiro, P. M. S., Munro, D. R., Nabel, J.

837   E. M. S., Nakaoka, S.-I., O'Brien, K., Olsen, A., Omar, A. M., Ono, T., Pierrot, D.,

838   Poulter, B., Rödenbeck, C., Salisbury, J., Schuster, U., Schwinger, J., Séférian, R.,

839   Skjelvan, I., Stocker, B. D., Sutton, A. J., Takahashi, T., Tian, H., Tilbrook, B., van

840   der Laan-Luijkx, I. T., van der Werf, G. R., Viovy, N., Walker, A. P., Wiltshire, A. J.,

841   and Zaehle, S.: Global Carbon Budget 2016, Earth Syst. Sci. Data, 8, 605-649,

842   https://doi.org/10.5194/essd-8-605-2016, 2016.

843   Landschützer, P., Gruber, N., Bakker, D. C. E., Schuster, U., Nakaoka, S., Payne, M. R.,

844   Sasse, T., and Zeng J., A neural network-based estimate of the seasonal to

845   inter-annual variability of the Atlantic Ocean carbon sink, Biogeosciences, 10, 7793–

846   7815, doi:10.5194/bg-10-7793-2013, 2013.

847   Landschützer, P., Gruber, N., Bakker, D. C. E., and Schuster, U.: Recent variability of

848   the global ocean carbon sink, Global Biogeochemical Cycles, 28, 927-949,

849   doi:10.1002/2014GB004853, 2014.

850   Lefèvre, N., Watson, A. J., and Watson, A. R.: A comparison of multiple regression and

851   neural network techniques for mapping in situ pCO_2 data, Tellus B, 57: 375–384.

852   doi:10.1111/j.1600-0889.2005.00164.x, 2005.

853   Lewis, E., and Wallace, D. W. R.: Program Developed for CO_2 System Calculations.

854   ORNL/CDIAC-105. Carbon Dioxide Information Analysis Center, Oak Ridge

855   National Laboratory, U.S. Department of Energy, Oak Ridge, Tennessee, 1998.

856   Lewis, K.M., Mitchell, B.G., van Dijken, G.L., and Arrigo, K.R.: Regional chlorophyll

857   a algorithms in the Arctic Ocean and their effect on satellite-derived primary

858   production estimates, Deep-Sea Res. II, 130, 17–24, doi:10.1016/j.dsr2.2016.04.020,

859   2016.

860   Loose, B., McGillis, W. R., Schlosser, P., Perovich, D., and Takahashi, T.: Effects of

861   freezing, growth, and ice cover on gas transport processes in laboratory seawater

862   experiments, Geophys. Res. Lett., 36, L05603, doi:10.1029/2008GL036318, 2009.

863   Lueker, T. J., Dickson, A. G., and Keeling, C. D.: Ocean pCO_2 calculated from

864   dissolved inorganic carbon, alkalinity, and equations for K1 and K2: validation based

865   on laboratory measurements of CO_2 in gas and seawater at equilibrium, Mar. Chem.,

866   70, 105–119, 2000.

867 Manizza, M., Follows, M. J., Dutkiewicz, S., Menemenlis, D., McClelland, J. W., Hill,

868   C. N., Peterson, B. J., and R. M. Key: A model of the Arctic Ocean carbon cycle, J.

869   Geophys. Res., 116, C12020, doi:10.1029/2011JC006998, 2011.

870 Maréchal, D., A soil-based approach to rainfall-runoff modelling in ungauged

871   catchments for England and Wales. PhD thesis, Cranfield University, U.K., 157 pp,

872   2004.

873 Maritorena, S., d'Andon, O. H. F., Mangin, A., and Siegel, D. A.: Merged satellite ocean

874   color data products using a bio-optical model: Characteristics, benefits and issues,

875   Remote Sensing of Environment, 114, 1791-1804, doi:10.1016/j.rse.2010.04.002,

876   2010.

877 Matsuoka, A., Huot, Y., Shimada, K., Saitoh, S., and Babin, M.: Bio-optical

878   characteristics of the western Arctic Ocean: Implications for ocean color algorithms,

879   Canadian J. Remote Sens., 33, 503–518, doi:10.5589/m07-059, 2007.

880 Meier, W., Fetterer, F., Savoie, M., Mallory, S., Duerr, R., and Stroeve, J.:

881   NOAA/NSIDC Climate Data Record of Passive Microwave Sea Ice Concentration.

882   Version 2, Boulder, Colorado USA: National Snow and Ice Data Center,

883 http://dx.doi.org/10.7265/N55M63M1, 2013.

884 Moore, T. S., Dowell, M. D., and Franz, B. A.: Detection of coccolithophore blooms in

885 ocean color satellite imagery: A generalized approach for use with multiple sensors,

886 Rem. Sens. Env., 117, 249–263, doi: 10.1016/j.rse.2011.10.001, 2012.

887 Mucci, A., Lansard, B., Miller, L. A., and Papakyriakou, T. N.: CO_2 fluxes across the

888 air-sea interface in the southeastern Beaufort Sea: Ice-free period, J. Geophys. Res.,

889 115, C04003, doi:10.1029/2009JC005330, 2010.

890 Murata, A.: Increased surface seawater pCO_2 in the eastern Bering Sea shelf: An effect

891 of blooms of coccolithophorid *Emiliania huxleyi*? Global Biogeochem. Cycles, 20,

892 GB4006, doi:10.1029/2005GB002615, 2006.

893 Murray, F. W.: On the computation of saturation vapor pressure. J. Applied Meteorology,

894 6, 203–204, 1967.

895 Nakaoka, S., Telszewski, M., Nojiri, Y., Yasunaka, S., Miyazaki, C., Mukai, H., and

896 Usui, N.: Estimating temporal and spatial variation of sea surface pCO_2 in the North

897 Pacific using a self organizing map neural network technique, Biogeosciences, 10,

898 6093-6106, doi:10.5194/bg-10-6093-2013, 2013.

899 Olsen, A., Brown, K. R., Chierici, M., Johannessen, T., and Neill, C.: Sea-surface CO_2

900 fugacity in the subpolar North Atlantic, Biogeosciences, 5, 535–547,

901   doi:10.5194/bg-5-535-2008, 2008.

902   Olsen, A., Key, R. M., van Heuven, S., Lauvset, S. K., Velo, A., Lin, X., Schirnick, C.,

903   Kozyr, A., Tanhua, T., Hoppema, M., Jutterström, S., Steinfeldt, R., Jeansson, E.,

904   Ishii, M., Pérez, F. F., and Suzuki, T.: The Global Ocean Data Analysis Project

905   version 2 (GLODAPv2) – an internally consistent data product for the world ocean,

906   Earth Syst. Sci. Data, 8, 297–323, 2016, doi:10.5194/essd-8-297-2016, 2016.

907   O'Reilly, J. E., Maritorena, S., Mitchell, B. G., Siegel, D. A., Carder, K. L., Garver, S. A.,

908   Kahru, M., and McClain, C.: Ocean color chlorophyll algorithms for SeaWiFS, J.

909   Geophys. Res., 103, 24937–24953, doi:10.1029/98JC02160, 1998.

910   Peng, G., Meier, W., Scott, D., and Savoie, M.: A long-term and reproducible passive

911   microwave sea ice concentration data record for climate studies and monitoring.

912   Earth Syst. Sci. Data 5: 311–318, http://dx.doi.org/10.5194/essd-5-311-2013, 2013.

913   Perrette, M., Yool, A., Quartly, G. D., and Popova, E. E.: Near-ubiquity of ice-edge

914   blooms in the Arctic, Biogeosciences, 8, 515–524, doi:10.5194/bg-8-515-2011, 2011.

915   Popova, E. E., Yool, A., Coward, A. C., Dupont, F., Deal, C., Elliott, S., Hunke, E., Jin,

916   M., Steele, M., and Zhang, J., What controls primary production in the Arctic Ocean?

917   Results from an intercomparison of five general circulation models with

918   biogeochemistry, J. Geophys. Res., 117, C00D12, doi:10.1029/2011JC007112, 2012.

919   Reynolds, R. W., Rayner, N. A., Smith, T. M., Stokes, D. C., and Wang, W.: An

920   improved in situ and satellite SST analysis for climate, J. Climate, 15, 1609–1625,

921   2002.

922   Schuster, U., McKinley, G. A., Bates, N., Chevallier, F., Doney, S. C., Fay, A. R.,

923   González-Dávila, M., Gruber, N., Jones, S., Krijnen, J., Landschützer, P., Lefèvre, N.,

924   Manizza, M., Mathis, J., Metzl, N., Olsen, A., Rios, A. F., Rödenbeck, C.,

925   Santana-Casiano, J. M., Takahashi, T., Wanninkhof, R., and Watson, A. J.: An

926   assessment of the Atlantic and Arctic sea–air CO_2 fluxes, 1990–2009,

927   Biogeosciences, 10, 607–627, doi:10.5194/bg-10-607-2013, 2013.

928   Shutler, J. D., Land, P. E., Brown, C. W., Findlay, H. S., Donlon, C. J., Medland, M.,

929   Snooke, R., and Blackford, J. C.: Coccolithophore surface distributions in the North

930   Atlantic and their modulation of the air-sea flux of CO_2 from 10 years of satellite

931   Earth observation data, Biogeosciences, 10, 2699–2709,

932   doi:10.5194/bg-10-2699-2013, 2013

933   Semiletov, I., Makshtas, A., Akasofu, S.-I., and Andreas, E. L: Atmospheric CO_2

934   balance: The role of Arctic sea ice, Geophys. Res. Lett., 31, L05121,

935   doi:10.1029/2003GL017996, 2004.

936   Semiletov, I. P., Pipko, I. I., Repina, I., and Shakhova, N. E.: Carbonate chemistry

937   dynamics and carbon dioxide fluxes across the atmosphere–ice–water interfaces in

938   the Arctic Ocean: Pacific sector of the Arctic, J. Mar. Syst., 66, 204–226,

939   doi:10.1016/j.jmarsys.2006.05.012, 2007.

940   Signorini, S. R., and McClain, C. R.: Effect of uncertainties in climatologic wind, ocean

941   pCO_2, and gas transfer algorithms on the estimate of global sea-air CO_2 flux, Global

942   Biogeochem. Cycles, 23, GB2025, doi:10.1029/2008GB003246, 2009.

943   Siswanto, E., Tang, J., Ahn, Y.-H., Ishizaka, J., Yoo, S., Kim, S.-W., Kiyomoto, Y.,

944   Yamada, K., Chiang, C., and Kawamura, H.: Empirical ocean color algorithms to

945   retrieve chlorophyll-a, total suspended matter, and colored dissolved organic matter

946   absorption coefficient in the Yellow and East China Seas, J. Oceanogr.,

947   doi:10.1007/s10872-011-0062-z, 2011.

948   Siswanto, E., Ishizaka, J., Tripathy, S. C., and Miyamura, K.: Detection of harmful algal

949   blooms of *Karenia mikimotoi* using MODIS measurements: a case study of

950   Seto-Inland Sea, Japan, Remote Sensing of Environment, 129, 185–196,

951   doi:10.1016/j.rse.2012.11.003, 2013.

952   Smyth, T. J., Tyrrell, T., Tarrant, B.: Time series of coccolithophore activity in the

953   Barents Sea, from twenty years of satellite imagery, Geophys. Res. Lett., 31, L11302,

954   doi:10.1029/2004GL019735, 2004.

955   Steele, M., Morley, R., and Ermold, W.: PHC: A global ocean hydrography with a high

956   quality Arctic Ocean, J. Climate, 14, 2079–2087, 2001.

957   Sweeney, C., Gloor, E., Jacobson, A. R., Key, R. M., McKinley, G., Sarmiento, J. L.,

958   and Wanninkhof, R.: Constraining global air-sea gas exchange for CO_2 with recent

959   bomb ^{14}C measurements, Global Biogeochem. Cycles, 21, GB2015,

960   doi:10.1029/2006GB002784, 2007.

961   Takahashi, T., Sutherland, S. C., Wanninkhof, R., Sweeney, C., Feely, R. A., Chipman,

962   D. W., Hales, B., Friederich, G., Chavez, F., Sabine, C., Watson, A., Bakker, D. C. E.,

963   Schuster, U., Metzl, N., Yoshikawa-Inoue, H., Ishii, M., Midorikawa, T., Nojiri, Y.,

964   Körtzinger, A., Steinhoff, T., Hoppema, M., Olafsson, J., Arnarson, T. S., Tilbrook,

965   B., Johannessen, T., Olsen, A., Bellerby, R., Wong, C. S., Delille, B., Bates, N. R., de

966   Baar, H. J. W.: Climatological mean and decadal changes in surface ocean pCO_2, and

967   net sea-air CO_2 flux over the global oceans. Deep-Sea Res. II, 56, 554–577, 2009.

968   Takahashi, T., Sutherland, S.C., and Kozyr, A.: Global Ocean Surface Water Partial

969   Pressure of CO_2 Database: Measurements Performed During 1957–2014 (Version

970   2014). ORNL/CDIAC-160, NDP-088(V2014). Carbon Dioxide Information Analysis

971   Center, Oak Ridge National Laboratory, U.S. Department of Energy, Oak Ridge,

972   Tennessee, doi: 10.3334/CDIAC/OTG.NDP088(V2014), 2015.

973   Tassan, S.: Local algorithms using SeaWiFS data for the retrieval of phytoplankton,

974   pigments, suspended sediment, and yellow substance in coastal waters, Applied Opt.,

975   33, 2369–2378, doi:10.1364/AO.33.002369, 1994.

976   Telszewski, M., Chazottes, A., Schuster, U., Watson, A. J., Moulin, C., Bakker, D.C.E.,

977   González-Dávila, M., Johannessen, T., Körtzinger, A., Lüger, H., Olsen, A., Omar, A.,

978   Padin, X. A., Ríos, A. F., Steinhoff, T., Santana-Casiano, M., Wallace, D. W. R., and

979   Wanninkhof, R.: Estimating the monthly pCO_2 distribution in the North Atlantic

980   using a self-organizing neural network, Biogeosciences, 6, 1405–1421,

981   doi:10.5194/bg-6-1405-2009, 2009.

982   Ulfsbo, A., Cassar, N., Korhonen, M., van Heuven, S., Hoppema, M., Kattner, G., and G.

983   Anderson, L.: Late summer net community production in the central Arctic Ocean

984   using multiple approaches, Global Biogeochem. Cycles, 28, 1129–1148,

985   doi:10.1002/2014GB004833, 2014.

986   van Heuven, S., Pierrot, D., Lewis, E., and Wallace, D. W. R.: MATLAB Program

987   Developed for CO2 System Calculations, ORNL/CDIAC-105b. Carbon Dioxide

988   Information Analysis Center, Oak Ridge National Laboratory, US Department of

989   Energy, Oak Ridge, Tennessee, 2009.

990   Wanninkhof, R.: Relationship between wind speed and gas exchange over the ocean, J.

991   Geophys. Res., 97(C5), 7373–7382, doi:10.1029/92JC00188, 1992.

992   Wanninkhof, R., Park, G. -H., Takahashi, T., Sweeney, C., Feely, R., Nojiri, Y., Gruber,

993   N., Doney, S. C., McKinley, G. A., Lenton, A., Le Quéré, C., Heinze, C., Schwinger,

994   J., Graven, H., and Khatiwala, S.: Global ocean carbon uptake: magnitude, variability

995   and trends, Biogeosciences, 10, 1983–2000, doi:10.5194/bg-10-1983-2013, 2013.

996   Wanninkhof, R.: Relationship between wind speed and gas exchange over the ocean

997   revisited, Limnol. Oceanogr.: Methods, 12, 351-362, 2014.

998   Weiss, R. F.: Carbon dioxide in water and seawater: the solubility of a non-ideal gas,

999   Mar. Chem., 2, 203–215, 1974.

1000   Yasunaka, S., Nojiri, Y., Nakaoka, S., Ono, T., Whitney, F. A., and Telszewski, M.:

1001   Mapping of sea surface nutrients in the North Pacific: Basin-wide distribution and

1002   seasonal to interannual variability, J. Geophys. Res. Oceans, 119, 7756–7771,

1003   doi:10.1002/2014JC010318, 2014.

1004   Yasunaka, S., Murata, A., Watanabe, E., Chierici, M., Fransson, A., van Heuven, S.,

1005   Hoppema, M., Ishii, M., Johannessen, T., Kosugi, N., Lauvset, S. K., Mathis, J. T.,

1006   Nishino, S., Omar, A. M., Olsen, A., Sasano, D., Takahashi, T., and Wanninkhof, R.:

1007   Mapping of the air–sea CO_2 flux in the Arctic Ocean and its adjacent seas:

1008   basin-wide distribution and seasonal to interannual variability, Polar Science, 10,

1009   323–334, doi:10.1016/j.polar.2016.03.006, 2016.

1010   Zeng, J, Nojiri, Y., Landschützer, P., Telszewski, M., Nakaoka, S.: A global surface

1011   ocean fCO$_2$ climatology based on a feed-forward neural network, Journal of

1012   Atmospheric and Ocean Technology, 31, 1838-1849,

1013   doi:10.1175/JTECH-D-13-00137.1, 2014.

Figure 1: Map of the Arctic Ocean and its adjacent seas. Gray contour lines show the 1000, 2000, 3000, and 4000 m isobaths. Blue lines show the 17-year annual mean position of the ice edge (SIC = 15 %). Area for the mapping is north of 60° N (heavy black circle). Sectors selected for regional analysis are the Arctic Ocean (dashed magenta line), the Greenland/Norwegian Seas (green 1), the Barents Sea (green 2), and the Chukchi Sea (green 3).

1032

1033

1034

1035

1036

1037

1038

1039

1040

1041

1042
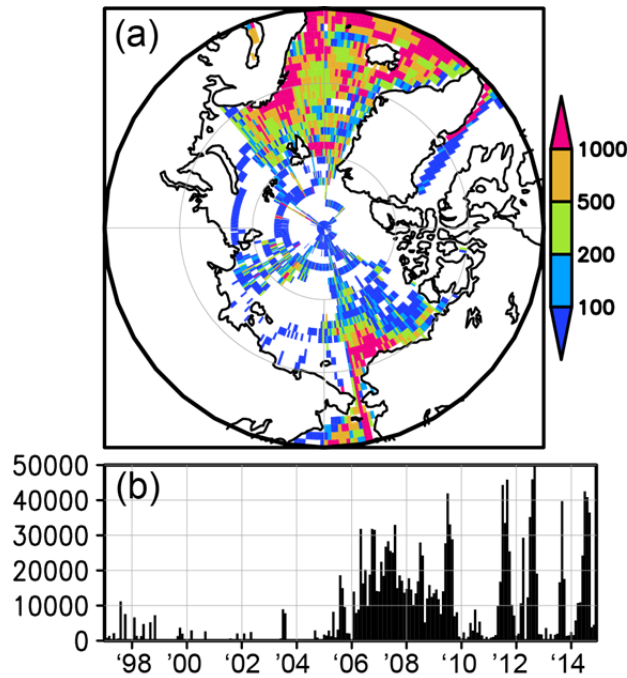
1043   Figure 2: (a) The number of ocean surface CO_2 data in the grid boxes (1° × 1°) used in

1044   this study. Data are from SOCATv4, LDEOv2014, GLODAPv2, and collected by R/V

1045   *Mirai* of JAMSTEC between 1997 and 2014. (b) Monthly number of CO_2 data in the

1046   analysis area (north of 60° N) from 1997 to 2014.

1047
1048
1049
1050
1051
1052
1053
1054

1055
1056
1057
1058
1059

1060

1061
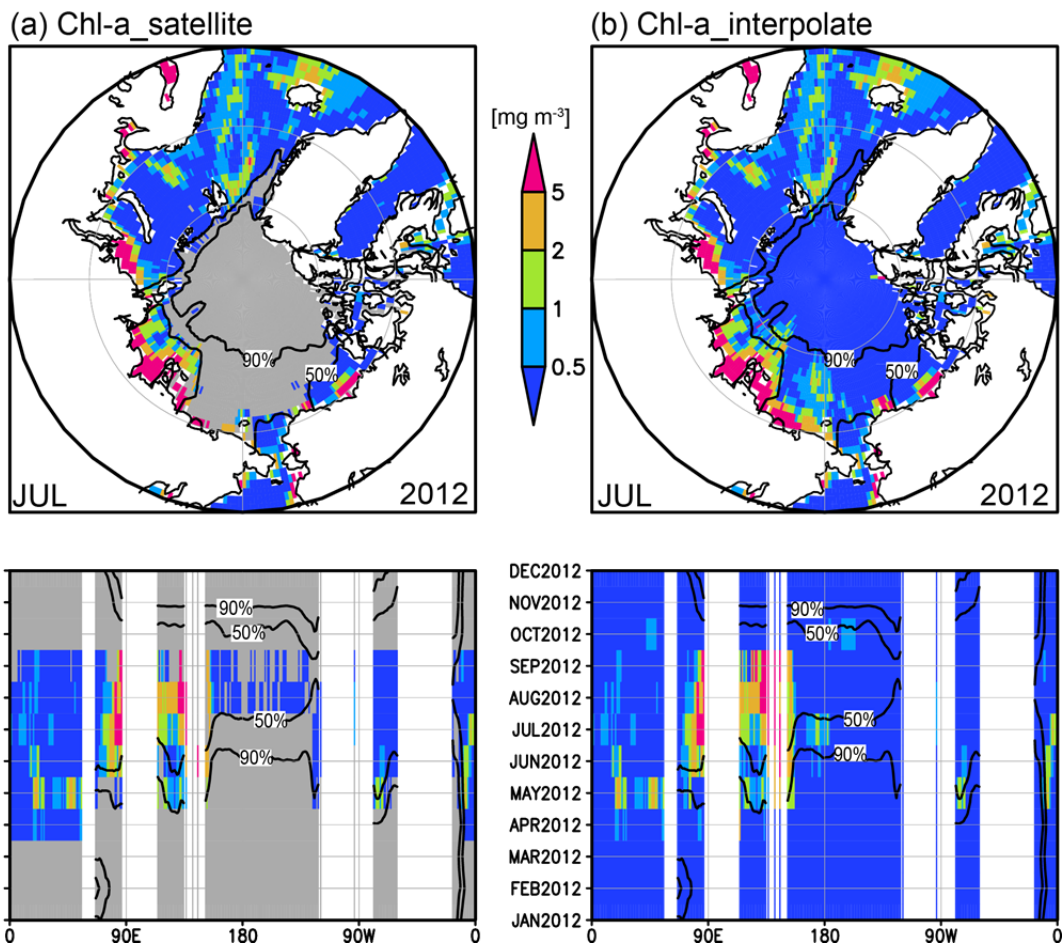
1062 Figure 3: (a) Original and (b) interpolated Chl-a [mg m^{-3}] in July 2012 (upper panels),

1063 and along 75°N in 2012 (lower panels). Black lines denote SIC of 50% and 90%. Gray

1064 areas in (a) indicate missing Chl-a data.
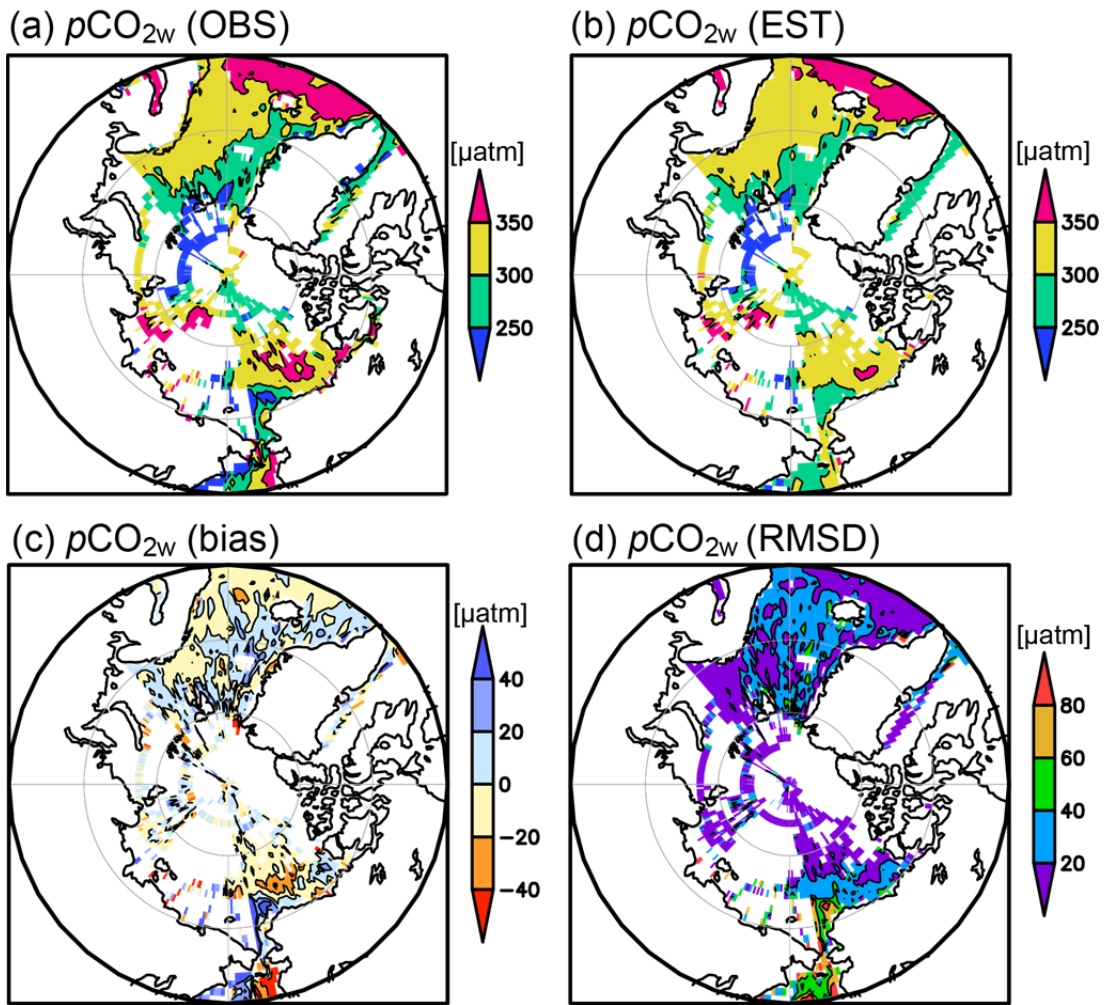
Figure 4: (a) Observed pCO_{2w} averaged over the whole analysis period [μatm]. (b)

Estimated pCO_{2w} averaged over the grid boxes in which observed pCO_{2w} values were

available [μatm]. (c) Bias (estimate–observation) and (d) root-mean-square-difference

between observed and estimated pCO_{2w} averaged over the whole analysis period

[μatm].
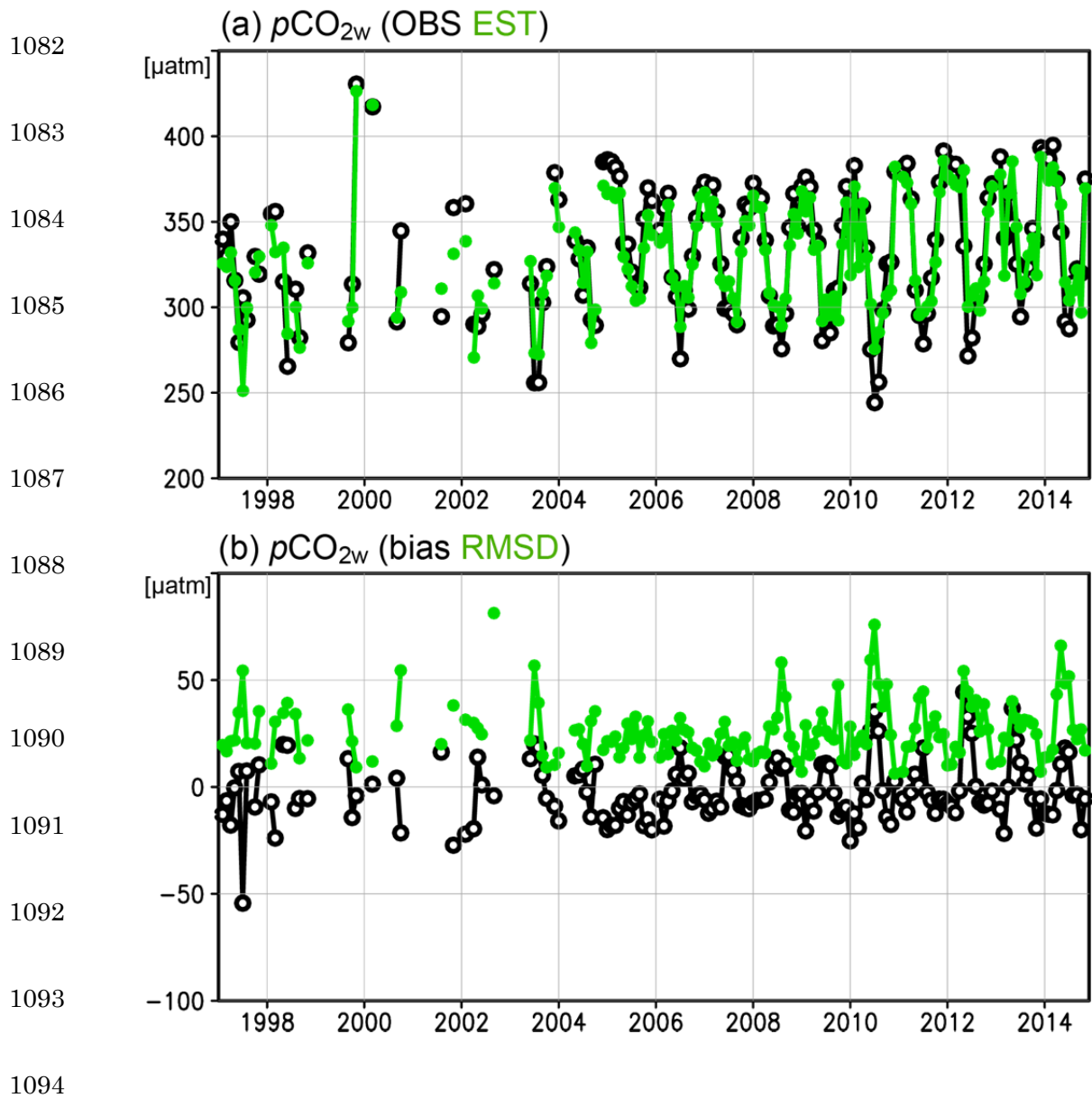
Figure 5: (a) Monthly time series of observed pCO_{2w} averaged over the entire analysis

area (black), and estimated pCO_{2w} averaged over the grid boxes in which observed

pCO_{2w} values were available (green) [µatm]. (b) Bias (estimate–observation; black) and

root-mean-square-difference (green) between observed and estimated pCO_{2w} averaged

over the entire analysis area [µatm].

1100

1101

1102

1103

1104

1105

1106

1107

1108

1109

1110
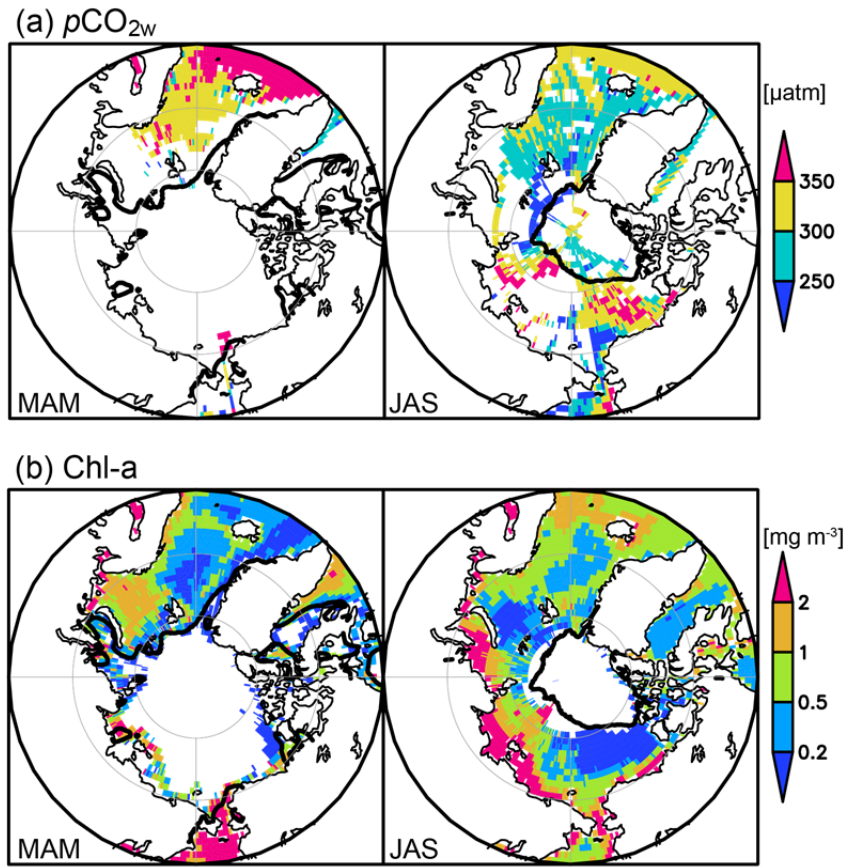
1111 Figure 6: (a) Observed pCO$_{2w}$ [µatm], and (b) non-interpolated Chl-a [mg m^{-3}] in

1112 March–May (left), and July–September (right) from 1997 to 2014.

1113

1124
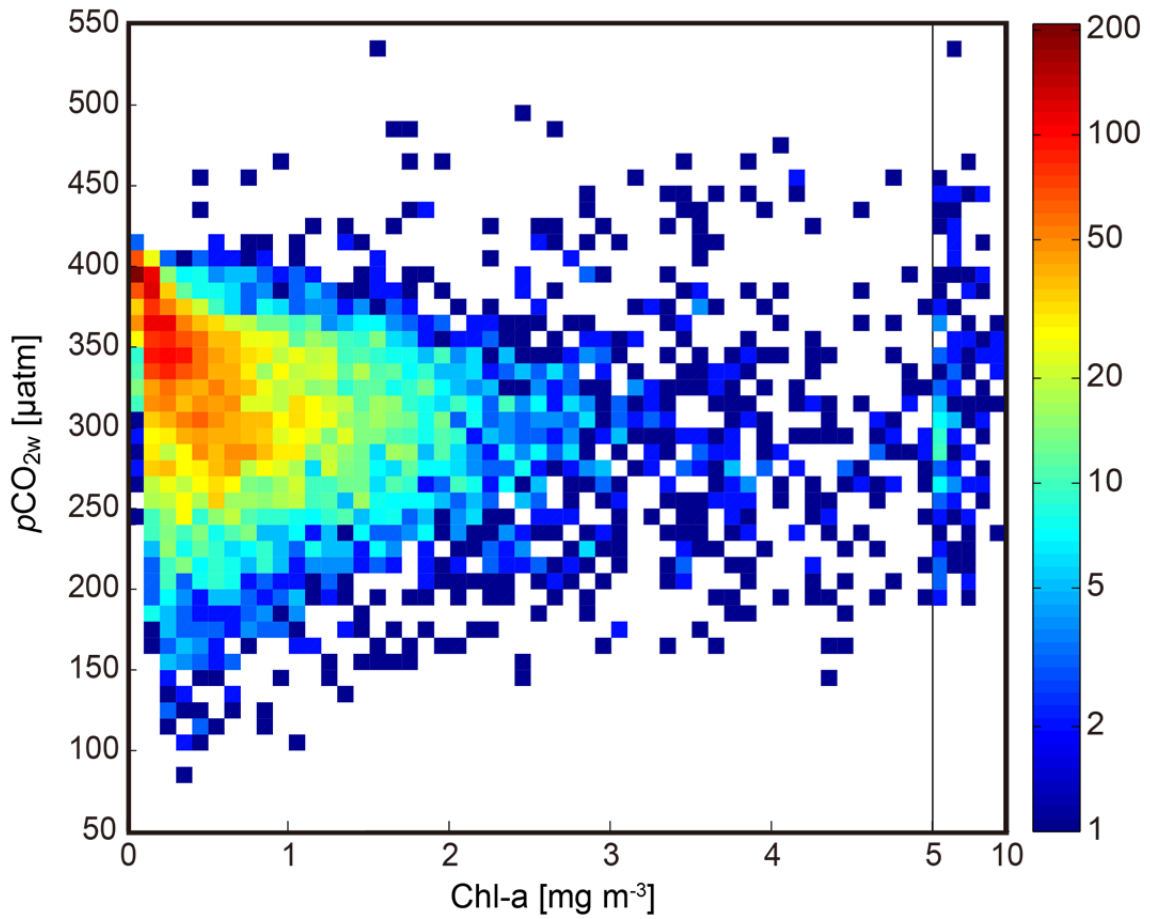
1125   Figure 7: Observed pCO$_{2w}$ [µatm] vs. satellite Chl-a [mg m^{-3}] in the Arctic Ocean and

1126   its adjacent seas (north of 60° N) from 1997 to 2014. Colors indicate the number of data

1127   pairs in a 0.1 mg m^{-3} × 5 µatm bin when Chl-a ≤ 5 mg m^{-3}, or in a 1 mg m^{-3} × 5 µatm

1128   bin when Chl-a > 5 mg m^{-3}.

1129

1130

1131

1132

1133

1134

1135

1136

1137

1138

1139
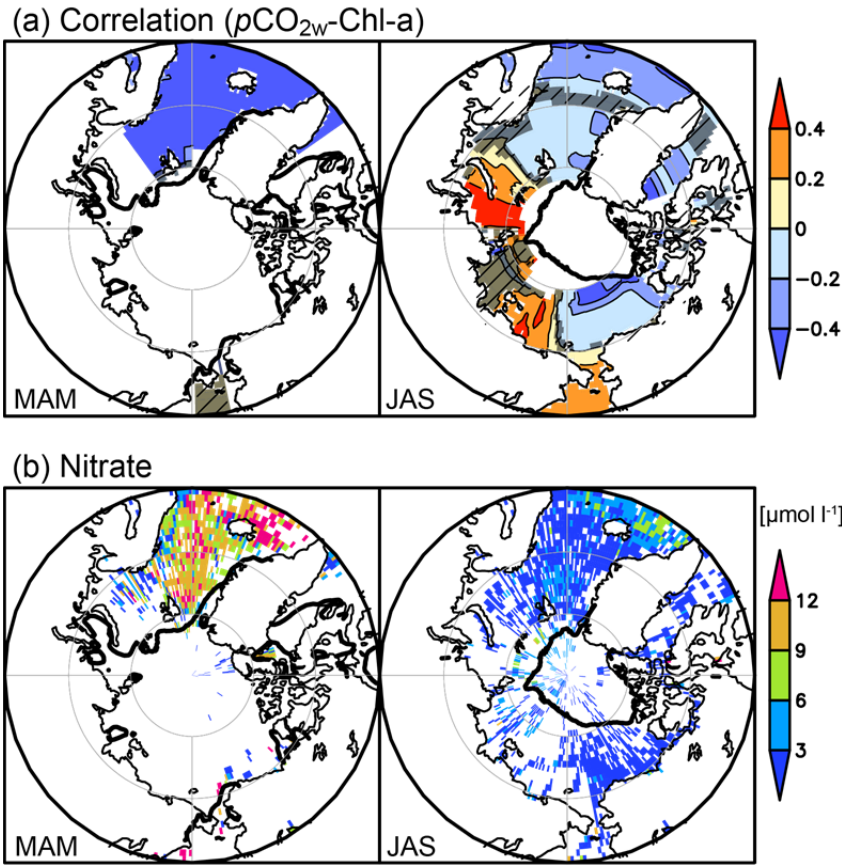
Figure 8: (a) Spatial correlation (correlation coefficient, r) between pCO$_{2w}$ and Chl-a in

a window size of ±1 month, ±5° of latitude, and ±30° of longitude in March–May (left),

and July–September (right). Darker hatched areas represent values in grids where

correlations are insignificant ($P > 0.05$). (b) Surface nitrate concentration [µmol l^{-1}] in

March–May (left), and July–September (right) from 1997 to 2014.

1146

1147

1148

1149

1150

1151

1152

1153

1154
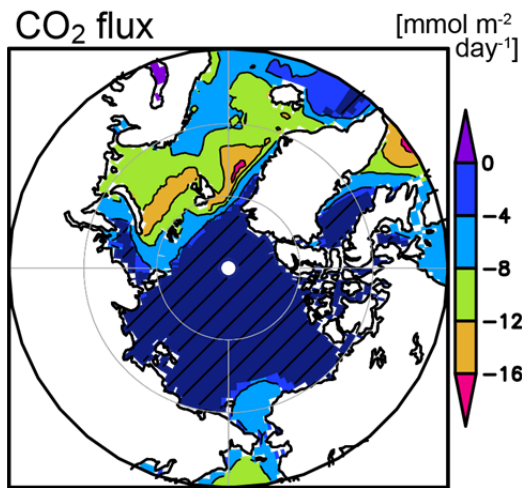
1155 Figure 9: Eighteen-year annual means of CO_2 flux [mmol m^{-2} day^{-1}] (negative values

1156 indicate flux into the ocean). Darker hatched areas represent show values in grids where

1157 fluxes were smaller than the uncertainty, estimated as described in the text.

1158

1159

1160

1161

1162

1163

1164

1165

1166

1167

1168

1169

1170
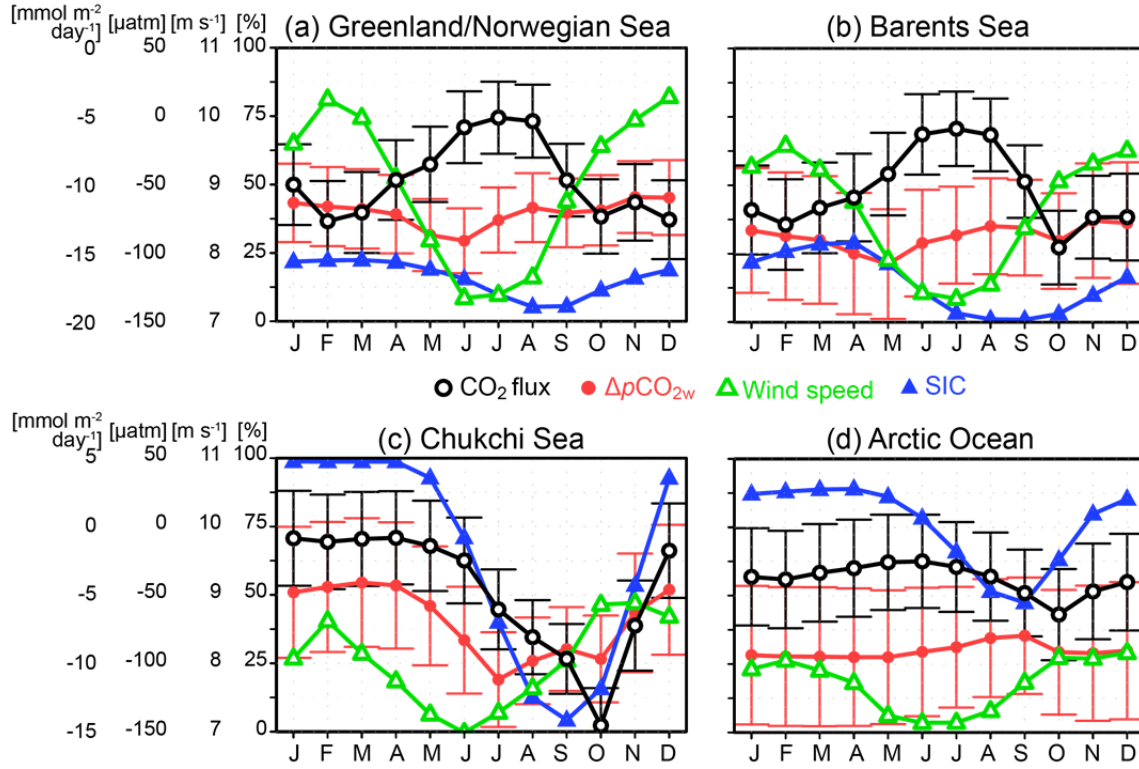
1171 Figure 10: Eighteen-year monthly mean CO_2 flux [mmol m^{-2} day^{-1}] (black), ΔpCO_2

1172 [µatm] (red), wind speed [m sec^{-1}] (green), and SIC [%] (blue), averaged over (a) the

1173 Greenland/Norwegian Seas, (b) the Barents Sea, (c) the Chukchi Sea, and (d) the Arctic

1174 Ocean. Error bars indicate the uncertainty.

1175

1176

1177

1178

1179

1180

1181

1182

1183

1184

1185

Figure 11: Area-mean interannual variations of CO_2 flux [mmol m^{-2} day^{-1}] (black), ΔpCO_2 [µatm] (red), wind speed [m sec^{-1}] (green), and SIC [%] (blue) in (a) the Greenland/Norwegian Seas, (b) the Barents Sea, (c) the Chukchi Sea, and (d) the Arctic Ocean. Error bars indicate the uncertainty.

1186

1187

1188

1189

1190

1191

1197

1202

1203
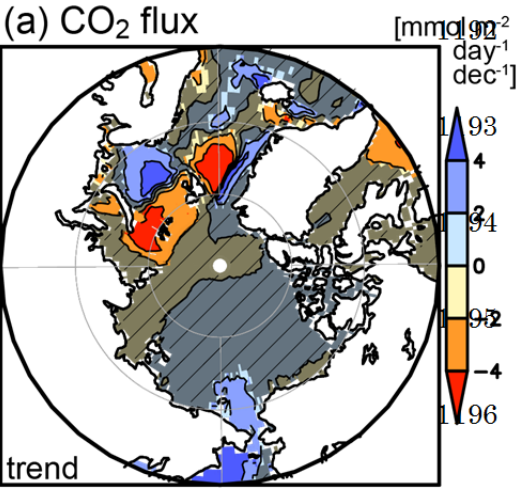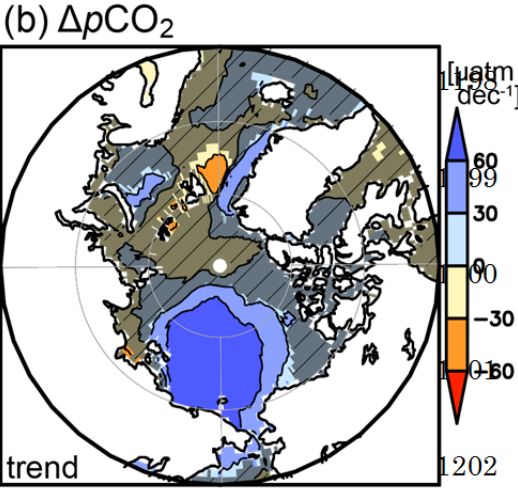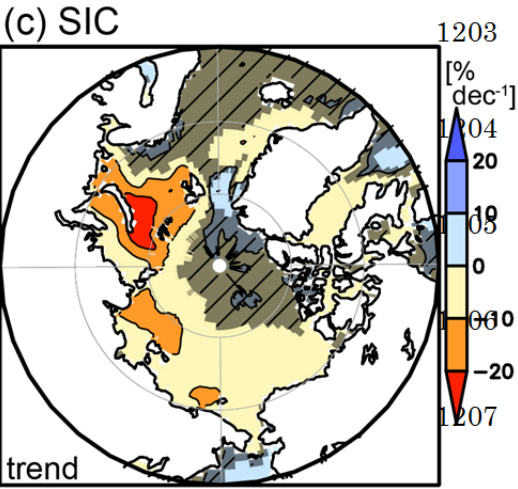
Figure 12: Trends in (a) CO_2 flux [mmol m^{-2} day^{-1} decade^{-1}], (b) $\Delta p CO_2$ [µatm decade^{-1}], and (c) SIC [% decade^{-1}]. Darker hatched areas represent values in grids where trend values were less than the uncertainty, estimated as described in the text.

1209

1210

1211

1212

1213

1214

1215

1216

1217

1218

1219

1220
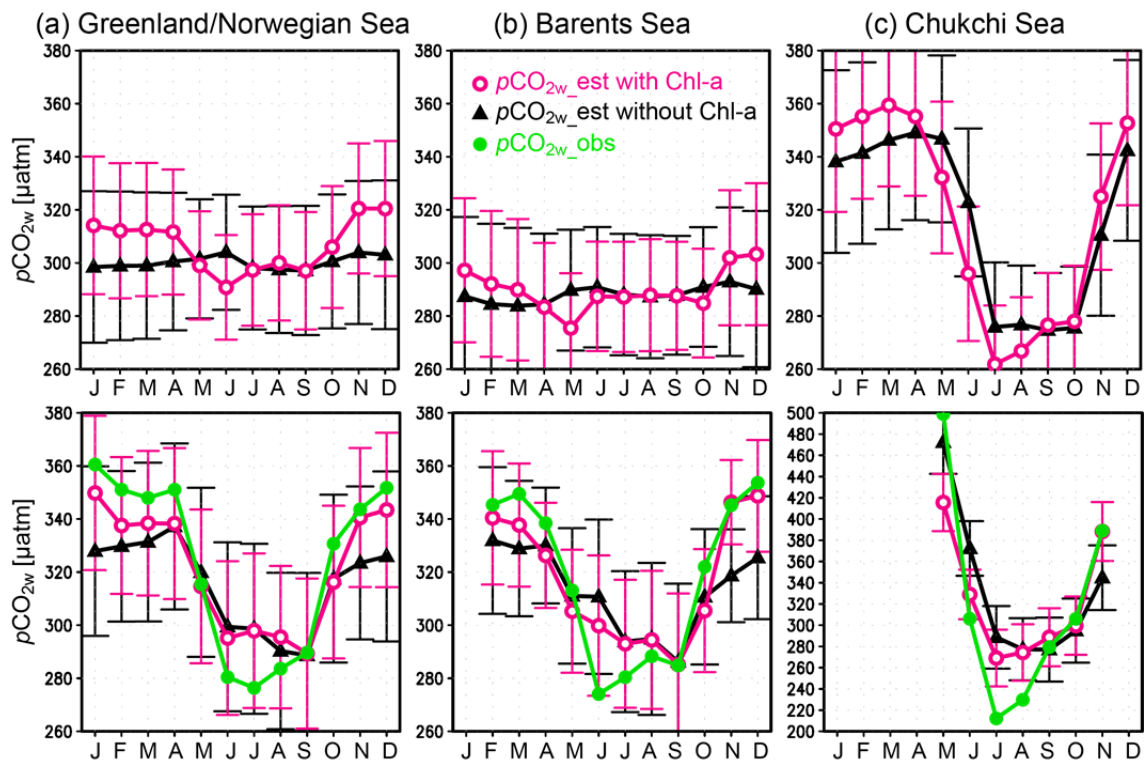
1221   Figure 13: Eighteen-year averaged pCO_{2w} seasonal variations [µatm] in (a) the

1222   Greenland/Norwegian Seas, (b) the Barents Sea, and (c) the Chukchi Sea. Black lines

1223   with triangles show estimates without Chl-a; magenta lines with open circles show

1224   estimates with Chl-a; green lines with closed circles show observed values. The upper

1225   panels show pCO_{2w} averaged for all grid cells with each region, and the lower panels

1226   show pCO_{2w} averaged over the grid boxes in which observed pCO_{2w} values were

1227   available. Error bars show the uncertainty, estimated as described in the text.

1228

1229

1230

1231

1232

1233

1234

1235

1236

1237

1238
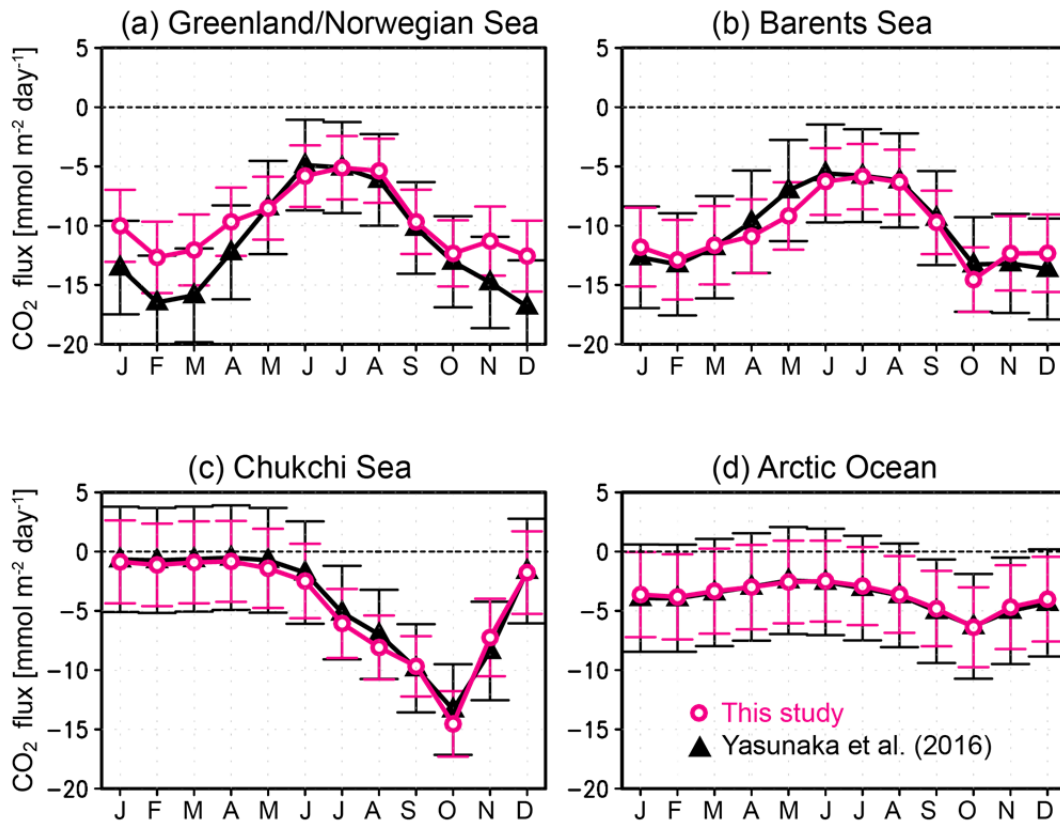
1239   Figure 14: Eighteen-year monthly mean CO_2 flux [mmol m^{-2} day^{-1}] averaged over (a)

1240   the Greenland/Norwegian Seas, (b) the Barents Sea, (c) the Chukchi Sea, and (d) the

1241   Arctic Ocean. Black lines with triangles show estimates without Chl-a by Yasunaka et al.

1242   (2016); magenta lines with open circles show estimates with Chl-a. Error bars show the

1243   uncertainty, estimated as described in the text.

1244

1245

1246 Table 1: RMSD [mg m^{-3}] and correlation (r) between Chl-a values

	standard algorithm		coastal algorithm	
	RMSD	r	RMSD	r
Chl-a from Arctic algorithm	0.80	0.90	0.81	0.87
Interpolated Chl-a from Arctic algorithm	0.37	0.92	0.48	0.86

1247

1248

1249